










## RESEARCH ARTICLE

10.1029/2024SW004108

# The Growth and Decay of Intense GNSS Amplitude and Phase Scintillation During Non-Storm Conditions

Mahith Madhanakumar<sup>1</sup> , Andres Spicher<sup>1</sup> , Juha Vierinen<sup>1</sup> , Kjellmar Oksavik<sup>2,3</sup> ,  
Anthea J. Coster<sup>4</sup>, Devin Ray Huyghebaert<sup>1,5</sup> , Carley J. Martin<sup>5</sup> , Ingemar Häggström<sup>6</sup>, and  
Larry J. Paxton<sup>7</sup> 

<sup>1</sup>Department of Physics and Technology, UiT The Arctic University of Norway, Tromsø, Norway, <sup>2</sup>Department of Physics and Technology, University of Bergen, Bergen, Norway, <sup>3</sup>Arctic Geophysics, University Centre in Svalbard, Longyearbyen, Norway, <sup>4</sup>Haystack Observatory, Massachusetts Institute of Technology, Westford, MA, USA, <sup>5</sup>Institute of Space and Atmospheric Studies, University of Saskatchewan, Saskatoon, SK, Canada, <sup>6</sup>EISCAT Scientific Association, Kiruna, Sweden, <sup>7</sup>The Johns Hopkins University Applied Physics Laboratory, Laurel, MD, USA

### Key Points:

- Intense amplitude and phase scintillation in the pre-noon sector during non-storm conditions
- Structuring down to Fresnel scales in both the auroral oval and inside the polar cap
- Depletion of Fresnel structures due to IMF  $B_z$  and  $B_y$  reversal in the post-noon sector

### Supporting Information:

Supporting Information may be found in the online version of this article.

### Correspondence to:

M. Madhanakumar,  
[mahith.madhanakumar@uit.no](mailto:mahith.madhanakumar@uit.no)

### Citation:

Madhanakumar, M., Spicher, A., Vierinen, J., Oksavik, K., Coster, A. J., Huyghebaert, D. R., et al. (2024). The growth and decay of intense GNSS amplitude and phase scintillation during non-storm conditions. *Space Weather*, 22, e2024SW004108. <https://doi.org/10.1029/2024SW004108>

Received 5 AUG 2024

Accepted 17 NOV 2024

### Author Contributions:

#### Conceptualization:

Mahith Madhanakumar, Andres Spicher

**Data curation:** Kjellmar Oksavik, Anthea J. Coster, Carley J. Martin,

Ingemar Häggström, Larry J. Paxton

**Formal analysis:** Mahith Madhanakumar

**Funding acquisition:** Andres Spicher

**Investigation:** Mahith Madhanakumar

**Methodology:** Mahith Madhanakumar

**Project administration:** Andres Spicher

**Software:** Mahith Madhanakumar

**Supervision:** Andres Spicher,

Juha Vierinen

**Validation:** Mahith Madhanakumar

**Visualization:** Mahith Madhanakumar

**Writing – original draft:**

Mahith Madhanakumar

**Writing – review & editing:**

Mahith Madhanakumar, Andres Spicher,

Juha Vierinen, Kjellmar Oksavik, Anthea

**Abstract** A multi-instrument study is conducted at the dayside polar ionosphere to investigate the spatio-temporal evolution of scintillation in Global Navigation Satellite System (GNSS) signals during non-storm conditions. Bursts of intense amplitude and phase scintillation started to occur at  $\sim 9$  MLT and persisted for more than 1 hour implying the simultaneous existence of Fresnel and large-scale sized irregularities of significant strength in the pre-noon sector. Measurements from the EISCAT radar in Svalbard (ESR) revealed the presence of dense plasma structures with significant gradients in regions of strong Joule heating/fast flows and soft precipitation when scintillation was enhanced. Plasma structuring down to Fresnel scales were observed both in the auroral oval as well as inside the polar cap with the associated amplitude scintillation exhibiting similar strengths regardless of whether the density structures were in regions of active auroral dynamics or not. The observations are placed within the context of different sources of free energy, providing insights into the important mechanisms that generate irregularities capable of perturbing GNSS signal properties in the dayside ionosphere. Furthermore, a strong negative excursion in the interplanetary magnetic field (IMF)  $B_y$  component during the northward turning of  $B_z$  led to the transport of a depleted region of plasma density into the post-noon sector that significantly weakened both amplitude and phase scintillation.

**Plain Language Summary** Ionospheric scintillation is a disturbance imposed by the ionosphere on radio signals of satellites in the form of rapid fluctuations in amplitude and phase. They are caused by electron density structures of varying sizes as they move across the path between a satellite signal and a ground based receiver. During strong scintillation, tracking signals become difficult thereby affecting technologies dependent on positioning, navigation and timing (PNT) services. It is therefore important to understand dynamics of the ionosphere that would result in enhanced scintillation in order to develop prediction or mitigation strategies for products using PNT information. In this study, we present evidence for the occurrence of intense amplitude and phase scintillation during quite geomagnetic conditions in the high latitude ionosphere. Our analysis revealed that large density structures propagating from lower latitudes can be modulated by different ionospheric processes such as fast flows and/or soft precipitation generating irregularities of varying scale-sizes which are associated with scintillation. Additionally, we also observed the depletion of irregularities in relation to the variation of interplanetary magnetic field components which, from a practical viewpoint, are beneficial for the users of satellites technologies and services due to the reduced impact of scintillation during such periods.

## 1. Introduction

Global Navigation Satellite Systems (GNSS) have become an integral part of our modern society with its services such as positioning, navigation and timing (PNT) finding application in a variety of fields ranging from personal navigation to agriculture, surveying, environmental modeling and aviation. Interruptions in GNSS services can arise when the signal properties are modified by plasma irregularities as the signal traverses the ionosphere (Kintner et al., 2001, 2007). Electron density irregularities frequently form in large-scale plasma structures with significant electron density gradients, leading to positioning errors that can even exceed 10 m at high latitudes during severe geomagnetic conditions (Yang et al., 2020). In addition to range errors, irregularities can also cause rapid fluctuations in the amplitude and phase of L-band signals, which is commonly referred to as scintillation

© 2024. The Author(s).

This is an open access article under the terms of the [Creative Commons Attribution License](https://creativecommons.org/licenses/by/4.0/), which permits use, distribution and reproduction in any medium, provided the original work is properly cited.

Attribution License, which permits use, distribution and reproduction in any medium, provided the original work is properly cited.

J. Coster, Devin Ray Huyghebaert, Carley  
J. Martín, Ingemar Häggström, Larry  
J. Paxton

(Yeh & Liu, 1982). Scintillation in the amplitude of a signal is due to diffraction of radio signals by Fresnel sized-irregularities, which are of the order of  $\sim 350$  m at 350 km for the GPS  $L_1$  frequency. On the other hand, perturbations in the signal phase can arise from diffractive fluctuations induced by Fresnel scaled irregularities (i.e., scintillation) and refractive fluctuations induced by large-scale irregularities convecting across the signal path with increased drift velocities at high latitudes (Kintner et al., 2007). In the literature, perturbations in phase due to both diffraction and refraction are collectively referred to as phase scintillation (Kintner et al., 2007). This paper will use the term Fresnel scaled irregularities to refer to small-scale irregularities that cause diffractive scintillation and large-scale irregularities to refer to density structures that predominantly causes refraction in GNSS signals. Even though refractive fluctuations from the phase can be corrected by using the ionosphere-free linear combination (IFLC), the technique fails to remove the ionospheric contribution during scintillation when diffractive contributions are simultaneously present (Carrano et al., 2013; McCaffrey & Jayachandran, 2019; Zheng et al., 2022). From the perspective of space weather impacts on GNSS technologies, both phase scintillation (diffractive + refractive) as well as amplitude scintillation are equally important. Intense phase scintillation can cause loss-of-lock in signals. On the other hand, simultaneous amplitude and phase scintillation can also result in loss-of-lock when tracking the phase plus deep amplitude fadings below the receiver threshold for continuous signal tracking, thereby impairing the technologies using GNSS receivers (Jiao & Morton, 2015; Jin & Oksavik, 2018; Liu et al., 2017; Semeter et al., 2017).

Scintillation studies at high latitudes have primarily reported phase scintillation in relation to polar cap patches, auroral structures, particle precipitation events and field-aligned currents (Alfonsi et al., 2011; Faehn Follestad et al., 2020; Forte et al., 2017; Jin et al., 2014, 2017; J. I. Moen et al., 2013; Oksavik et al., 2015; Smith et al., 2008; Prikryl et al., 2011; van der Meeren et al., 2015). Even though phase scintillation occurs more predominantly than amplitude scintillation at high latitudes, there have been some studies that focused on the simultaneous occurrence of amplitude and phase scintillation events. For instance, using the total electron content (TEC) and scintillation data collected during the Halloween storms of 2003, De Franceschi et al. (2008), Mitchell et al. (2005) showed amplitude and phase scintillation to be co-located in regions of large TEC gradients in the nightside sector. The climatology study over northern Europe by Spogli et al. (2009) revealed the enhancement of  $S_4$  index at the noon and midnight sectors under both quiet and disturbed geomagnetic conditions. Using GPS  $L_1$  data from the Canadian High Arctic Ionospheric Network (CHAIN), Meziane et al. (2020) investigated the seasonal and solar cycle dependence of amplitude scintillation during the 24th solar cycle revealing a maximum occurrence value of  $\sim 11\%$  during the early winter periods of high solar activity. Thayyil et al. (2021) reported significant amplitude and phase scintillation in relation to a polar cap patch at the nightside sector where non-linear evolution of the gradient drift instability mechanism was suggested to be responsible for generating Fresnel scale structures throughout the patch. Using observations from Skibotn in northern Norway, Jin and Oksavik (2018) studied strong amplitude and phase scintillation together with power fading and signal loss-of-locks associated with TEC blobs during the severe storm on St.Patrick's Day in 2015. A multi-instrument approach to investigating the favorable conditions triggering amplitude scintillation in the southern hemisphere during the main phase of a severe geomagnetic storm in September 2017 was conducted by D'Angelo et al. (2021). They suggested high ionization levels and strong plasma dynamics as the necessary conditions for amplitude scintillation occurrence. Using scintillation indices at 1-s resolution, Nishimura et al. (2023) associated amplitude and phase scintillation with different auroral forms at the nightside sector during a substorm. Cardenas-O'Toole et al. (2024) observed moderate levels of amplitude and phase scintillation at the dayside convection reversal boundary and which coincided with regions of large flow shear and enhanced soft electron precipitation.

As mentioned above, a large fraction of studies observed amplitude scintillation during periods of severe geomagnetic disturbances in the noon or nightside sectors of the high latitude ionosphere. Less attention has been paid to understanding the ionospheric effects on GNSS signals during weak or quite geomagnetic periods (i.e., when  $\text{SYM}H \geq -80$  nT following the definition of a weak storm in Hutchinson et al. (2011)). In this study, we present evidence for the occurrence of intense amplitude and phase scintillation in the pre-noon sector along with a significant reduction of scintillation in the post-noon sector during non-storm conditions on November 2013. The analysis was carried out using co-ordinated observations from a network of both ground and space based instruments that revealed the spatio-temporal evolution of irregularities of different scale-sizes and the associated scintillation in GNSS signals at the dayside high latitude ionosphere.

The outline of the paper is as follows. In Section 2, we provide an overview of the data and different instruments used in the study. In Section 3, the methodology employed to combine observations from multiple instruments is

discussed followed by the results in Section 4. Discussion of the results are offered in Section 5 with the key points summarized in the conclusions of Section 6.

## 2. Data and Instrumentation

Being a multi-instrument study we make use of a number of space-borne and ground-based instruments to characterize scintillation in GNSS signals at the high latitude ionosphere. An overview of the instruments (or data sources) used in the study is given below with a quick summary given in Table A1.

### 2.1. EISCAT Svalbard Radar (ESR)

Ionospheric parameters such as electron density ( $N_e$ ), electron temperature ( $T_e$ ), ion temperature ( $T_i$ ) and line-of-sight plasma velocity ( $V_i$ ) are collected from a wide range of latitudes by the steerable 32-m ESR dish operated in a scanning mode with a minimum elevation of  $30^\circ$  above the horizon (Wannberg et al., 1997). As the radar was simultaneously moving in azimuth, data from different longitude sectors are also available in this mode. Each scan is completed in about 12 minutes yielding *fan plots* of  $N_e$ ,  $T_e$ ,  $T_i$  and  $V_i$  as a function of altitude and latitude, produced with an integration time of  $\sim 30s$  (Carlson et al., 2002). Data with errors greater than 40% are discarded from the analysis. Additionally, the measurements from the co-located field-aligned ESR-42 m, produced with an integration time of  $\sim 60s$ , are used to complement the observations from ESR-32 m. The ESR measurements are analyzed using the GUIDAP toolbox (Lehtinen & Huuskonen, 1996).

### 2.2. GNSS Ionospheric Scintillation and TEC Monitors (GISTM)

Scintillation and TEC data primarily used in this study are collected by a NovAtel GPStation-6 GNSS Ionospheric Scintillation and TEC Monitor (GISTM) installed at the Kjell-Henrikson Observatory (KHO) in Longyearbyen. This receiver is capable of simultaneously tracking signals at several different frequencies and from different constellations including GPS, GALILEO and GLONASS (Oksavik, 2020a). Amplitude and phase scintillation indices ( $S_4, \sigma_\phi$ ) together with TEC and ROT data with 60-s resolution are the primary data sets used from this instrument. These 60-s resolution indices are calculated and recorded automatically by the receiver. The  $S_4$  index is calculated from raw amplitude whereas a sixth-order Butterworth high-pass filter is used to detrend raw phase and calculate the  $\sigma_\phi$  index (Fremouw et al., 1978; Van Dierendonck et al., 1993). Vertical TEC is obtained from slant TEC assuming an ionospheric pierce point (IPP) at 350 km (Horvath & Crozier, 2007). Additionally, raw carrier phase and amplitude, recorded at a sampling rate of 50 Hz, were used to re-calculate  $S_4$  and  $\sigma_\phi$  indices at 1-s resolution. Using the 1-s window would allow us to better capture the intense and short-lived bursts in scintillation that otherwise would be averaged out if using the traditional 1-min window. Similar to the 60-s resolution indices, the 1-s  $S_4$  was calculated from raw power whereas  $\sigma_\phi$  at 1-s resolution was obtained from the detrended phase. Only data corresponding to elevation angles greater than  $40^\circ$  are considered to avoid multipath effects. More information about data processing can be found in Oksavik et al. (2015) and van der Meeren et al. (2015). When presenting TEC maps, scintillation and TEC data collected by the receivers in Bjørnøya (BJN) and Ny-Ålesund (NYA) are additionally used to expand the data coverage. These data set are part of The University of Bergen GNSS Data Collection (Oksavik, 2020b).

### 2.3. Madrigal Total Electron Content (TEC)

The plasma variability at global scales are captured using the GPS vertical TEC data from the Madrigal database (Coster, 2013). Bins of  $1^\circ \times 1^\circ$  in geographical latitude-longitude, generated every 5 min, contain VTEC values that are calculated from the line-of-sight TEC assuming an ionospheric slab at 350 km altitude (Rideout & Coster, 2006). Methods implemented to compute GPS receiver biases for TEC measurements in the Madrigal database are described in Vierinen et al. (2016). In this study we use data from latitude ranges of  $60^\circ$ – $90^\circ$  to generate TEC maps in Magnetic Local Time (MLT) and Altitude-Adjusted Corrected Geomagnetic (AACGM-v2) coordinates. The readers are referred to Shepherd (2014) and Burrell et al. (2020) for more information on AACGM-v2 co-ordinates as well as for converting between geographic and geomagnetic co-ordinates.

### 2.4. Super Dual Auroral Radar Network (SuperDARN)

SuperDARN is a network of globally distributed High Frequency (HF) coherent scatter radars used to image large-scale ionospheric convection and plasma dynamics in the polar, auroral, sub-auroral and mid-latitude

regions (Chisham et al., 2007; Nishitani et al., 2019). Two dimensional  $\mathbf{E} \times \mathbf{B}$  velocity of the high latitude plasma is measured by observing the drift of field-aligned irregularities in the F region (Ruohoniemi & Baker, 1998). Data from the northern hemisphere radars are used to generate maps of velocity and electric potential using the SuperDARN community “Radar Software Toolkit” (SuperDARN Data Analysis Working Group, 2022). In this study we only use data covering a latitude range of  $60^\circ - 90^\circ$  in the MLT - AACGM-v2 coordinates (Burrell et al., 2020; Shepherd, 2014; SuperDARN Data Visualization Working Group, 2024). Together with the TEC maps, use of SuperDARN data allows association of the global evolution of the ionospheric flow to the movement of large density structures in the polar ionosphere.

### 2.5. Special Sensor Ultraviolet Spectrographic Imager (SSUSI)

SSUSI is a far ultraviolet (UV) instrument consisting of a Spectrographic Imaging System (SIS) mounted on a nadir-looking panel of the Defense Meteorological Satellite Program (DMSP) satellites F16-F19, that are in a nearly polar, sun-synchronous orbits at an altitude of about 850 km. SSUSI records UV emissions from the Earth's upper atmosphere in five wavelength bands in the spectral range 115–180 nm by scanning across the track of the DMSP trajectory every 15 s (Paxton et al., 1992, 2002). In this study, we make use of the poleward and equatorward auroral boundary locations obtained from the Auroral Environmental Data Record (EDR).

### 2.6. OMNI

In order to study the impact of Interplanetary Magnetic Field (IMF) on the ionospheric dynamics and hence on GNSS scintillation we make use of the 1-min high resolution OMNI data set timeshifted to the nose of Earth's bow shock (King & Papitashvili, 2005). Of particular relevance to this study are the IMF  $B_y, B_z$  components in Geocentric Solar Magnetospheric (GSM) coordinates, solar wind flow speed and pressure. Additionally, as a proxy for the geomagnetic storm strength, the 1-min resolution SYMH index that captures the disturbances in the symmetric horizontal component, H, is used (World Data Center for Geomagnetism, Kyoto, 2022). The Auroral Electrojet (AE), Auroral Upper (AU) and Auroral Lower (AL) indices with 1-min resolution are used to capture the ionospheric disturbances at high latitudes (World Data Center for Geomagnetism, Kyoto, 2015).

## 3. Methodology

In this section, we briefly outline the procedure developed to combine and present the data sets from different sources. The  $S_4$  and  $\sigma_\phi$  of a given PRN were calculated from all the available frequencies. In this study, we used the maximum value of the  $S_4$  and  $\sigma_\phi$  to capture the maximum level of scintillation at any given time period.  $S_4$  values are corrected for noise by using the equation (Van Dierendonck et al., 1993):

$$S_4 = \sqrt{S_{4tot}^2 - S_{4cor}^2} \quad (1)$$

where  $S_{4tot}$  is the total  $S_4$  that include contributions from both ionosphere and the ambient noise whereas  $S_{4cor}$  is the correction to total  $S_4$  due to the effect of ambient noise. An event is classified as amplitude scintillation if  $S_4 \geq 0.1$  and phase scintillation if  $\sigma_\phi \geq 0.1$  rad. Due to Fresnel filtering effect, the dominant contribution to amplitude scintillation comes from irregularities with scale-sizes of the order of couple of hundreds of meters or less whereas irregularities with scale-sizes ranging from several meters to kilometers can contribute to phase scintillation (Forte & Radicella, 2002; Yeh & Liu, 1982).

All TEC maps are overplotted with  $S_4$  values whereas SuperDARN convection maps contain  $\sigma_\phi$  values (see Figures 2–4). In addition, the zoomed versions of the TEC maps also contain the look directions of the scanning ESR-32 m beams as gray dotted lines and the field-aligned ESR-42 m beams as purple lines. Since the TEC maps are of 5 min resolution and the scintillation indices are of 1-min resolution, the maximum value of the scintillation indices during every 5 min interval, for each PRN, are only overplotted for clarity and to avoid cluttering. Since the SuperDARN maps are of 2 min resolution, the average of the convection pattern and velocities during each 5 min interval is taken. In addition, the convection maps also show the poleward and equatorward edges of the auroral boundary obtained from DMSP SSUSI. If there are data from multiple DMSP satellites corresponding to

any TEC timestamp, the average of the boundary locations are taken. Furthermore, in cases when there are no data, we use the boundary locations corresponding to the nearest TEC timestamp when data was available. The IMF  $B_y, B_z$  clock plots are also shown alongside the TEC maps.

When presenting the ESR-32 m fan plots (see Figure 5),  $S_4$  values are always overplotted on top of  $N_e$  and  $T_e$  scans whereas  $T_i$  and  $V_i$  plots contain the  $\sigma_\phi$  values. Conjunctions between GNSS signals and scanning radar beams are identified using the procedure outlined in Madhanakumar et al. (2024). In our study, a conjunction is defined to occur if a PRN link falls within a (lat, lon) threshold of  $(\pm 0.5^\circ, \pm 2^\circ)$ , at an IPP of 350 km, of a radar beam. A similar procedure is used to identify conjunctions between the field-aligned ESR-42 m and GNSS signals. By integrating the densities observed by the ESR-42 m along each beam, the corresponding TEC values are calculated which are then converted to vertical TEC ( $VTEC^{radar}$ ). In addition, the gradients in density are obtained using the following equation:

$$\nabla N_e = \frac{\Delta N_e}{\Delta x} \quad (2)$$

where  $\Delta x = v \times \Delta t$ . Here,  $\Delta N_e = N_e(t_{i+1}) - N_e(t_i)$ ,  $\Delta t = t_{i+1} - t_i$ ,  $v$  = average velocity of plasma flow in a  $2 \times 2$  grid of (lat, lon) around the ESR-42 m location obtained from SuperDARN. Note that  $\nabla N_e$  corresponds to the component of density gradient along the  $\mathbf{E} \times \mathbf{B}$  drift direction.

## 4. Results

Having given a brief overview of the methodology, we now proceed to present the results of the multi-instrument study aimed to characterize intense levels of amplitude and phase scintillation during non-storm conditions. We first present the prevailing IMF conditions and the corresponding scintillation observations from KHO. Subsequently, we show the behavior of the ionosphere at global scales and its response to the IMF  $B_y, B_z$  components. Finally, we show the persisting ionospheric conditions above Svalbard during different intervals of scintillation.

### 4.1. IMF and Scintillation/TEC Behavior

Panels (a–d) of Figure 1 presents the IMF conditions during the 7<sup>th</sup> of November 2013 together with the SYMH and AE indices. Figure 1c shows negative excursions in the SYMH index implying some enhancements in the ring current activity. However, as discussed in Gonzalez et al. (1994), every ring current enhancement cannot be considered as a signature of storm level disturbances. Hutchinson et al. (2011) classified a storm as weak if  $-150 < SYMH \leq -80$  nT. Since the minimum value of SYMH index observed in our study was only  $-52$  nT, our event does not even fall within the definition of a weak storm. We therefore consider our event as a typical example of a non-storm event. The 1-min resolution scintillation indices,  $S_4$  and  $\sigma_\phi$ , from all the satellites in the field-of-view during the given day are shown on panels (e–f) whereas the corresponding VTEC and ROT values are on panels (g–h). Three intervals separated in time were selected to illustrate the spatio-temporal evolution of the scintillation strength, beginning with a state of low activity followed by a period of intensification and a final reduction to background levels. These intervals are labeled (A), (B) and (C) respectively and are shaded in different colors to aid visual clarity (see Figure 1). Interval (A) corresponds to the time period between 03:30–06:00 UTC ( $\sim 06:30$ – $09:00$  MLT), interval (B) between 06:00–09:00 UTC ( $\sim 09:00$ – $12:00$  MLT) and interval (C) between 11:00–13:00 UTC ( $\sim 14:00$ – $16:00$  MLT). Relative to the average cusp location, interval A is therefore in the morning sector, interval B is distributed between the prenoon and noon sectors whereas interval C is in the afternoon sector.

During interval (A), IMF  $B_z$  was negative reaching a minimum value of  $-8$  nT at 05:20 UTC. The SYMH index starts decreasing in this interval after a prior increase. The AE index increases and reaches a maximum of  $\sim 1000$  nT indicating substorm activity. The  $S_4$  index remained below the threshold of 0.1 majority of the times whereas  $\sigma_\phi$  fluctuated between 0.05 and 0.2 rad on average (see also Figure B1).

In interval (B), IMF  $B_z$  remained southward majority of the times even though there were some small northward excursions. On the other hand, though the  $B_y$  component exhibited some negative turnings reaching a minimum

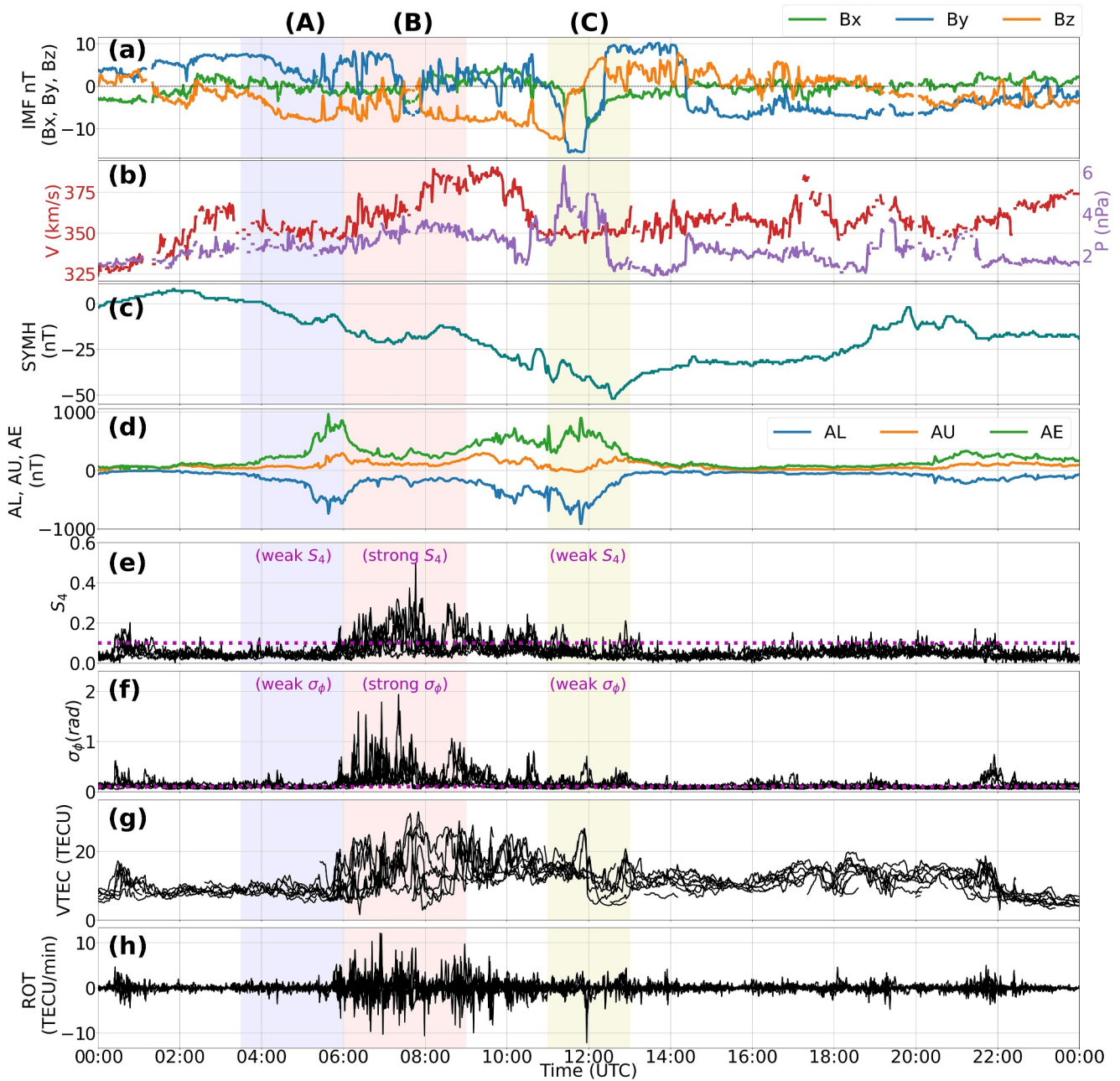


**Figure 1.** Interplanetary magnetic field conditions (panels a–b), SYMH index (panel c), auroral electrojet indices (panel d),  $S_4$ ,  $\sigma_\phi$  indices (panels e–f), GNSS VTEC and ROT (panels g–h) on 07 November 2013. In panels (e–h), data from all available PRNs have been included and a magenta dotted horizontal line in panels (e–f) show the threshold of 0.1 used to separate scintillation events from non-scintillation ones. The average scintillation intensities during the three intervals, (A), (B), (C), have been categorized as “weak” or “strong” to facilitate easy comparison of scintillation strengths across intervals.

value of about  $-7$  nT at 07:40 UTC, it remained mostly positive. The solar wind velocity is seen to increase during this interval reaching a maximum value of 390 km/s whereas the SYMH index barely exceeded  $-20$  nT. The AE index decreased and remained below 450 nT majority of the time. It is during this interval when intense levels of amplitude and phase scintillation were observed. As seen in panels (e–f), both  $S_4$  and  $\sigma_\phi$  simultaneously experienced bursts in scintillation that lasted for  $\sim 1$  hr reaching a maximum value of 0.5 and 1.9 rad respectively. The VTEC and ROT panels also showed significant enhancements from the background with the VTEC reaching a maximum value of 30 TECU whereas ROT maximized at 12 TECU/min. In addition, as shown in Figure B1 of the

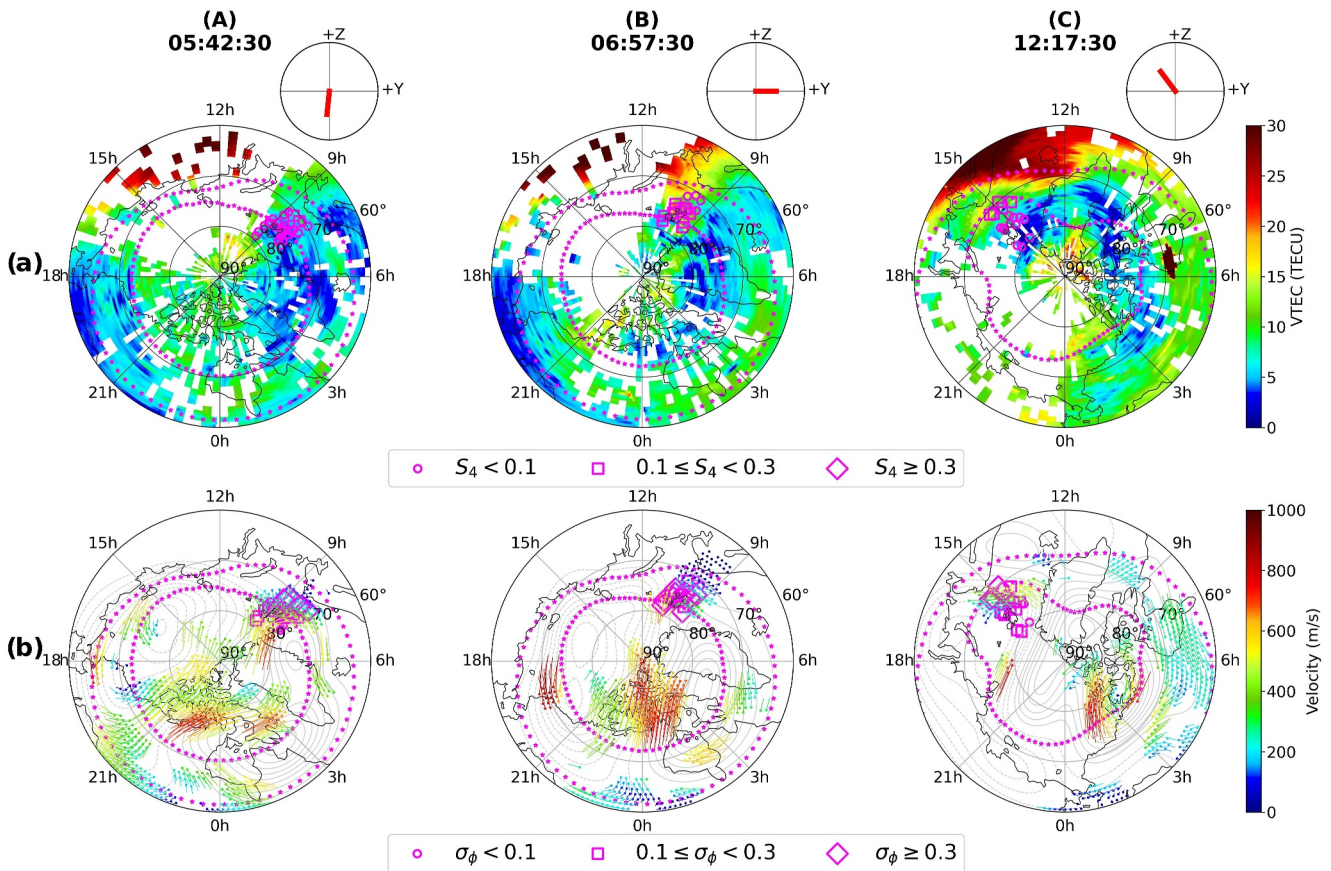


**Figure 2.** Panel (a): TEC maps corresponding to times within the same three intervals (A), (B), (C) as in Figure 1. Panel (b): SuperDARN convection maps along with poleward and equatorward auroral boundaries.  $S_4$  indices are overlotted on the TEC maps whereas  $\sigma_\phi$  values are overlaid on the SuperDARN maps. The interplanetary magnetic field clock plots are shown for each timestamps above the TEC maps.

appendix, the 1-s amplitude and phase scintillation indices showed larger enhancements than the 1-min indices with  $S_4$  and  $\sigma_\phi$  reaching a maximum value of 0.75, 2.2 rad respectively confirming that interval (B) was the most intense period of scintillation during the day.

Finally, interval (C) corresponds to the time period when IMF  $B_z$  turned positive after reaching a minimum value of  $-13$  nT at 11:15 UT and thereafter staying positive or around zero until 19:00 UT after which it further starts decreasing.  $B_y$  was strongly negative during this interval reaching a minimum of  $-15.5$  nT at 11:30 UT beyond which it flipped back to positive values of about 10 nT at 12:20 UT. This interval is associated with a region of enhanced solar wind pressure and a reduction in the solar wind velocity with the SYMH index reaching the minimum value of  $-52$  nT. The AE index was again enhanced reaching a maximum value of 900 nT indicating ongoing substorm activity in the nightside ionosphere. The  $S_4$  and  $\sigma_\phi$  strengths are observed to fade out during this interval with  $S_4 < 0.1$  on majority of the GNSS links whereas  $\sigma_\phi$  remained above the threshold though with reduced intensity as compared to interval (B). Clear differences in the magnitudes of VTEC and ROT are also seen in comparison to interval (B).

#### 4.2. Global Behavior

In order to investigate the global ionospheric behavior during the aforementioned three intervals, we make use of the global TEC and SuperDARN convection maps. These maps are shown in Figure 2 which also contain the IMF clock plots as well as the poleward and equatorward auroral boundaries from DMSP SSUSI. In addition, the  $S_4$

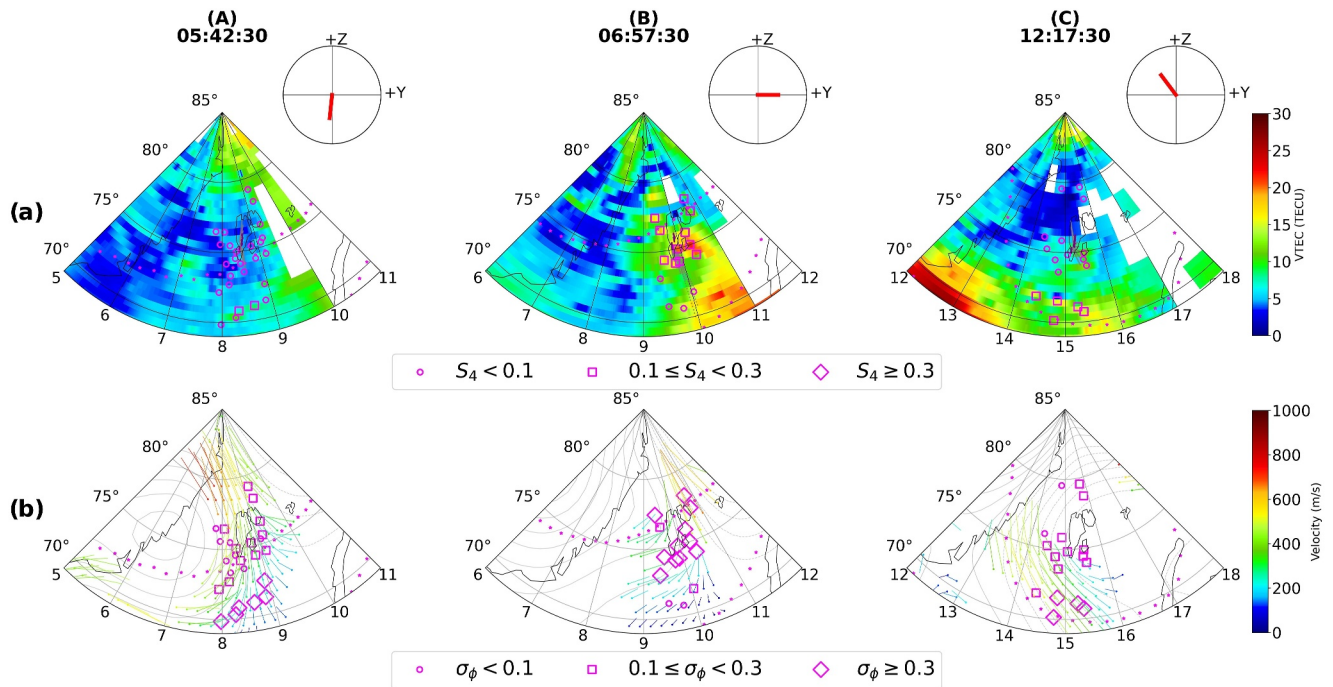


**Figure 3.** Zoomed in version of the TEC and SuperDARN maps above Svalbard with scintillation indices and DMSP SSUSI auroral boundaries overplotted. The interplanetary magnetic field clock plots are shown for each timestamps above the TEC maps.

and  $\sigma_\phi$  values are overplotted on top of the TEC and SuperDARN maps respectively. As mentioned earlier, for a given time and PRN, the maximum of  $S_4$  and  $\sigma_\phi$  values from the available frequencies are used. A zoomed in version of the TEC and SuperDARN maps above Svalbard archipelago, in the same format as Figure 2, is shown in Figure 3.

During interval A,  $B_y$  is mostly positive and hence the cusp is shifted toward later MLT bringing the interval further into the early morning local time. As seen in Figure 2b, enhanced regions of flow were visible in the dawn sector in the vicinity of the GNSS signals. Weak-moderate  $\sigma_\phi$  was observed on GNSS links whereas  $S_4$  remained below 0.1 majority of the times. As seen in Figure 3b, moderate  $\sigma_\phi$  occurred near the inflow region and inside the auroral oval whereas  $\sigma_\phi$  remained weak poleward and inside the polar cap. The corresponding TEC values in the vicinity remained low and varied between 5 and 10 TECU.

In interval B,  $B_y$  switches sign multiple times moving the cusp back and forth between prenoon and postnoon sectors (i.e., inside and outside the Svalbard field of view) making interval B the one when Svalbard was most favorably located relative to the cusp auroral region. This interval corresponds to the period when scintillation was simultaneously present in both amplitude and phase of the traversing GNSS radio signals. The TEC maps in Figures 2 and 3 show high density plasma structures in the field-of-view of multiple PRNs with the TEC values varying between 20 and 30 TECU in the immediate vicinity of the satellite links. Together with Movies S1 and S2 it is clear that these dense plasma structures originated at sub-auroral latitudes and then propagated poleward intersecting the raypaths of the PRNs. Figure 4 shows the snapshots of the TEC and SuperDARN maps corresponding to different timestamps during interval (B). Large plasma density enhancements are seen in the eastern half of the field of view (around 11:00 MLT) where the cusp inflow region is located. Significant enhancements in both  $S_4$  and  $\sigma_\phi$  were observed both in the auroral oval as well as inside the polar cap as multiple density structures convected across the paths of different GNSS signals into the polar cap. As compared to interval (A), Figure 3b shows that majority of the strongest phase scintillation during interval (B) now occurs poleward at higher latitudes even though dense plasma was present also at lower latitudes near the estimated equatorward edge of the boundary (from DMSP SSUSI).



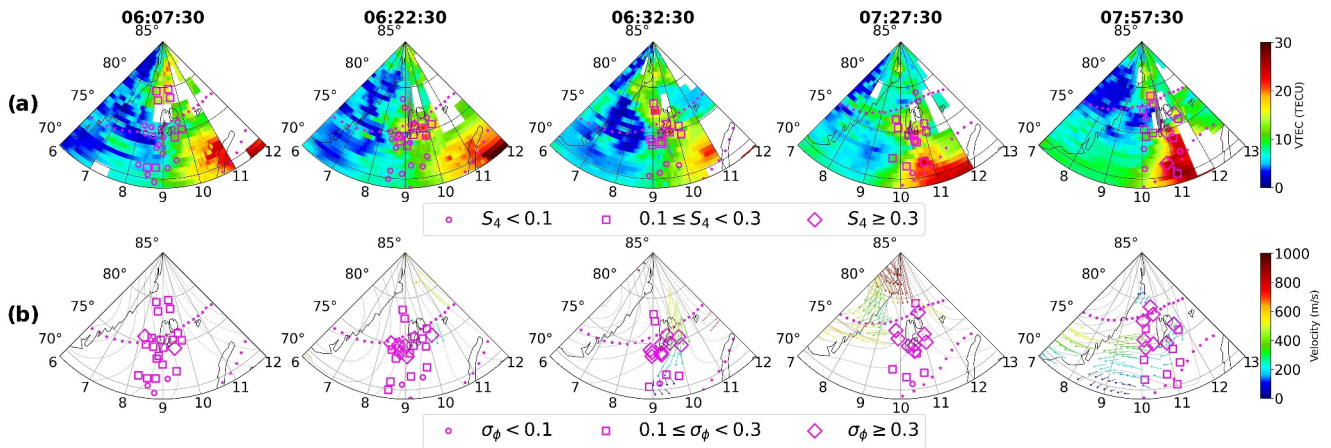


**Figure 4.** Enhancement in amplitude, phase scintillation inside both the auroral oval and polar cap during interval (B) as multiple high density structures propagated poleward from the sub-auroral latitudes.

In interval (C), we show the global ionospheric response when IMF  $B_y$  turned negative and  $B_z$  turned northward (see subsection 4.1 for precise IMF values). Since  $B_y$  is strongly negative, the cusp is shifted toward the prenoon MLT bringing the interval further into the late afternoon local time. As seen in Figure 2a, a depleted region of low density with TEC values ranging between 3 and 10 TECU formed in the polar ionosphere. A closer look in Figure 3a reveals that the intensity of both  $S_4$  and  $\sigma_\phi$  diminished significantly with  $S_4$  reduced to values below the threshold of 0.1 whereas  $\sigma_\phi$  became very weak. It is worth noting the persistence of both amplitude and phase scintillation at lower latitudes where fast flows and TEC gradients were still observed to exist.

### 4.3. Local Ionospheric Conditions

In order to capture the ionospheric conditions of the polar ionosphere during the different intervals of scintillation in detail, we make use of data from the 32 m EISCAT Svalbard radar (ESR-32 m). As mentioned in Section 2.1, measurements from the ESR-32 m were collected by operating it under the scanning mode allowing us to infer the ionospheric properties between  $\sim 70^\circ - 82^\circ$  magnetic latitudes during a 12 minute period. Figure 5 shows the ESR-32 m scan plots for times within the same three different intervals as in Figure 1, that is, before (interval A), during (interval B) and after (interval C) the intense period of simultaneous amplitude and phase scintillation.

During interval (A), the ESR was probing the polar ionosphere with low VTEC but enhanced flow conditions. The average F region electron density in the radar field-of-view and within the conjunction zone was  $\sim 6.5 \times 10^{10} \text{el}/\text{m}^3$ . As seen in Figures 5a and 5b amplitude scintillation was absent whereas Figures 5c and 5d show weak phase scintillation near regions of enhanced  $T_i$  and  $T_e$ . A channel of enhanced ion velocity directed toward the radar was present close to the region of enhanced  $T_i$ . The associated ion velocity exceeded 500 m/s in agreement with the SuperDARN flow velocities. Notably, a region of fast flow was also observed poleward of the radar without much enhancement in  $T_i$  and outside the conjunction zone of GNSS signals.

Interval (B) corresponds to the period when intense amplitude and phase scintillation were observed in multiple GNSS signals. Regions of enhanced densities were observed both equatorward and poleward of the radar's field of view with GNSS conjunction occurring only at equatorward latitudes. It is clear from Figure 5a that, during this interval, both  $S_4$  and  $\sigma_\phi$  were enhanced in regions of significant plasma densities with the average F region density equaling  $\sim 3.2 \times 10^{11} \text{el}/\text{m}^3$ . Furthermore, enhanced scintillation was co-located with narrow regions of enhanced  $T_e$  as well  $T_i$  as seen in Figures 5b and 5c. The line-of-sight ion velocity was low inside the conjunction zone but was enhanced at latitudes poleward of the radar.

In interval (C), a decrease in the electron density was observed with an average value of  $\sim 7 \times 10^{10} \text{el}/\text{m}^3$  within the conjunction zone at F region altitudes. Even though the ionosphere was still active with enhanced levels of  $T_e, T_i$ , panels (a), (b) show the absence of amplitude scintillation whereas weak phase scintillation persisted during this interval as seen in panels (c), (d).

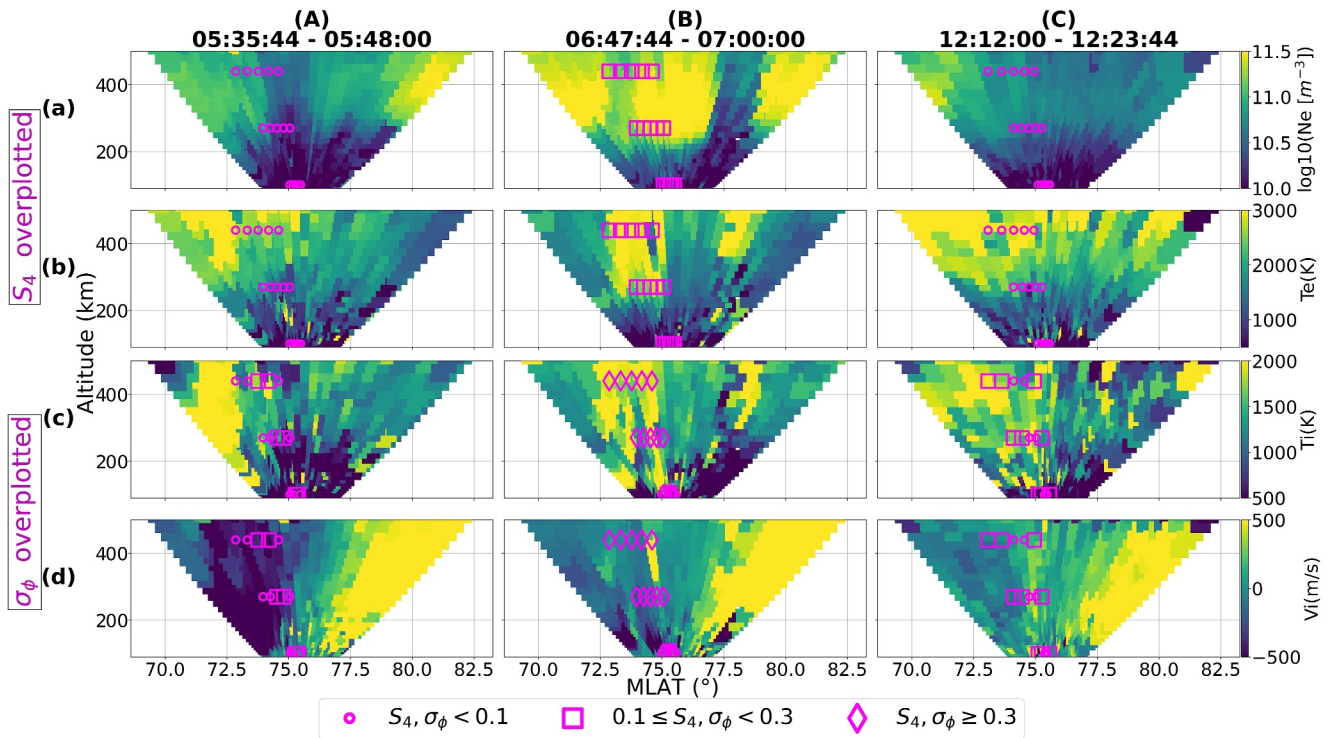


**Figure 5.** The ESR-32 m fan plots displaying the altitudinal profiles of  $N_e$  (panel a),  $T_e$  (panel b),  $T_i$  (panel c),  $V_i$  (panel d). Positive  $V_i$  values correspond to plasma velocities away from the radar. The fan plots correspond to times within the same three intervals (A), (B), (C) as in Figure 1. Also note that  $S_4$  indices are overplotted on panels (a), (b) whereas  $\sigma_\phi$  values are presented on panels (c), (d).

## 5. Discussion

Combining observations from the set of instruments discussed, the previous section showed the different stages of scintillation development and the associated ionospheric conditions in the polar ionosphere during non-storm conditions. Three different intervals were chosen to showcase the evolution of scintillation from a period of low activity to an intense state followed by the gradual fading in the intensity back to background levels.

### 5.1. Interval (A)

During interval (A), IMF  $B_z$  was southward for an extended period of time resulting in the equatorward expansion of the convection cells and auroral boundaries (Cowley & Lockwood, 1992). The corresponding  $B_y$  component remained mostly positive with the convection cells tilted toward the pre-noon pre-midnight direction (see Figure 1a for the  $B_y$  values and Figure 2b for the convection pattern). This orientation of the cells during positive  $B_y$  conditions shifts the throat/inflow region (i.e., the entry point of plasma into the polar cap) toward earlier MLTs and is consistent with the findings in Ruohoniemi and Greenwald (1996), Jin et al. (2015). As seen in Figures 2 and 3, signals from multiple GNSS satellites were in regions of enhanced velocities associated with both the sunward return flow as well as the anti-sunward poleward flow channels even though the associated TEC values were very low. For a time series evolution of the TEC and flow patterns see the Movies S1 and S2. As seen in Figures 1e, 1f, and B1, although there were some moderate bursts in  $\sigma_\phi$ , the average phase scintillation activity during this interval remained weak whereas amplitude scintillation remained absent or weak majority of the times. The ESR-32 m scans in Figure 5 as well in Movie S3 show an active ionosphere especially with enhanced  $T_i$  and fast flows. Enhancements in  $T_i$  in regions of enhanced velocities can be attributed to Joule heating of the ions due to its collision with neutrals (e.g., St-Maurice & Hanson, 1982; Skjæveland et al., 2017). The absence of enhanced  $S_4$  can then be attributed to the lack of enhanced densities or sufficient TEC in the vicinity of the GNSS radio signals. Weak phase without amplitude scintillation then implies that variations in the signal phase were

refractive in origin caused by rapid convection of plasma irregularities across the field of view of the GNSS signals (e.g., McCaffrey and Jayachandran (2019), Madhanakumar et al. (2022)).

## 5.2. Interval (B)

In interval (B), the TEC maps in Figures 2–4 as well as Movies S1 and S2 revealed the presence of large density structures at sub-auroral latitudes which often developed into patches as a result of detachment from the tongue of ionization (TOI). These structures had the same density as the subauroral plasma with enhancements at least twice the background values and propagated poleward in the anti-sunward direction. J. Moen et al. (2006) had also observed similar high density plasma structures at sub-auroral latitudes propagating toward the cusp inflow region using the EISCAT VHF radar. Depending on their location, they are called polar cap patches or blobs if found within or outside the polar cap respectively (Basu et al., 1990; Crowley et al., 2000). As we are only interested on the effects of these dense plasma structures on GNSS signals and not on the distinction between patches or blobs, we would collectively refer to these large density structures as patches for simplicity. Even though many mechanisms have been proposed to explain the formation of patches from high density reservoirs such as solar-EUV produced plasma and Storm Enhanced Densities (SED), it is beyond the scope of this work to investigate the exact structuring mechanism of the observed patches. Readers interested in the different formation mechanisms are referred to Sojka et al. (1993), Milan et al. (2002), Zhang et al. (2011), Carlson et al. (2006) and references therein. During this interval, Figures 4 and 5 show the poleward propagation of a series of patches with velocities varying between 400 and 700 m/s and which intersected regions of active soft precipitation (visible as enhanced  $T_e$  at F region altitudes) and enhanced flows/Joule heating (see also Movie S3). Intense bursts in both amplitude and phase scintillation were observed on multiple GNSS links in both the auroral oval and polar cap implying the simultaneous existence of both Fresnel and large-scale sized irregularities. Assuming a satellite velocity of  $\sim 20$  m/s and that the relative drift occurs along the horizontal direction, similar to Forte and Radicella (2002), together with an average irregularity drift of 550 m/s obtained from SuperDARN, the range of irregularity scale-sizes varied between  $\sim 50$  m - 3 km during periods of scintillation. Jin et al. (2017) observed strongest GPS phase scintillation associated with the combination of polar cap patches and auroral dynamics, followed by moderate scintillation in the case of cusp dynamics without polar cap patches, and weak scintillation with patches outside the cusp aurora. In this study, we also observed the phase scintillation to be the strongest in the oval whereas it remained moderate inside the polar cap majority of the times. Moreover, the strength of amplitude scintillation remained in the weak-moderate regime in both the auroral oval as well as inside the polar cap suggesting that the convecting dense plasma maintained the small-scale structuring irrespective of whether the patches were in regions of auroral dynamics or not. Thayyil et al. (2021) had similarly observed patches maintaining the integrity of Fresnel structures in the leading edge as they convected across nightside the polar cap. The Movie S3 shows some events where the 1-min  $S_4$  index was below 0.1 even though dense plasma was present in regions of enhanced  $T_e$  and  $T_i$ . However, the 1-s  $S_4$  was enhanced and remained above the threshold of 0.1 for these events. This discrepancy between the 1-s and 1-min indices could be because of the fact that the scintillation events were short lived and the 1-min index missed these intense bursts as a result of averaging over a larger window. The enhancement in the 1-s  $S_4$  index then suggests that Fresnel sized irregularities were in fact present during such events. At the nightside sector, Nishimura et al. (2023) had similarly observed the 1-s  $S_4$  index to be a better proxy than the 1-min index to capture the intense and short-lived bursts in amplitude scintillation associated with various auroral forms. Jiao et al. (2013) had observed amplitude scintillation events to be brief and lasting only for 3.7 min in duration. Even though small-scale irregularities have shorter life-span and dissipate faster, we however observed amplitude scintillation (and hence small-scale irregularities) to persist for more than 1 hour in duration.

In order to complement the observations made by the ESR-32 m, we also used the measurements from the field-aligned ESR-42 m. Figure 6 shows the measurements collected by the ESR-42 m for the same day and covering the same three intervals (A), (B), (C). Together with the usual ionospheric parameters  $N_e$ ,  $T_e$ ,  $T_i$ ,  $V_i$ , panel (b) shows the gradients in electron density ( $\nabla N_e$ ) whereas the vertical TEC from radar density measurements ( $VTEC^{radar}$ ) is plotted on panel (a) alongside  $N_e$ . The gradients were calculated from the electron density measurements using Equation 2 and following the procedure described in the methodology section. There is increased noise below 200 km due to a technical problem which however does not affect our results or discussions. Panels (f) and (g) contain the scintillation indices,  $S_4$  and  $\sigma_\phi$ , which are only plotted during times when there

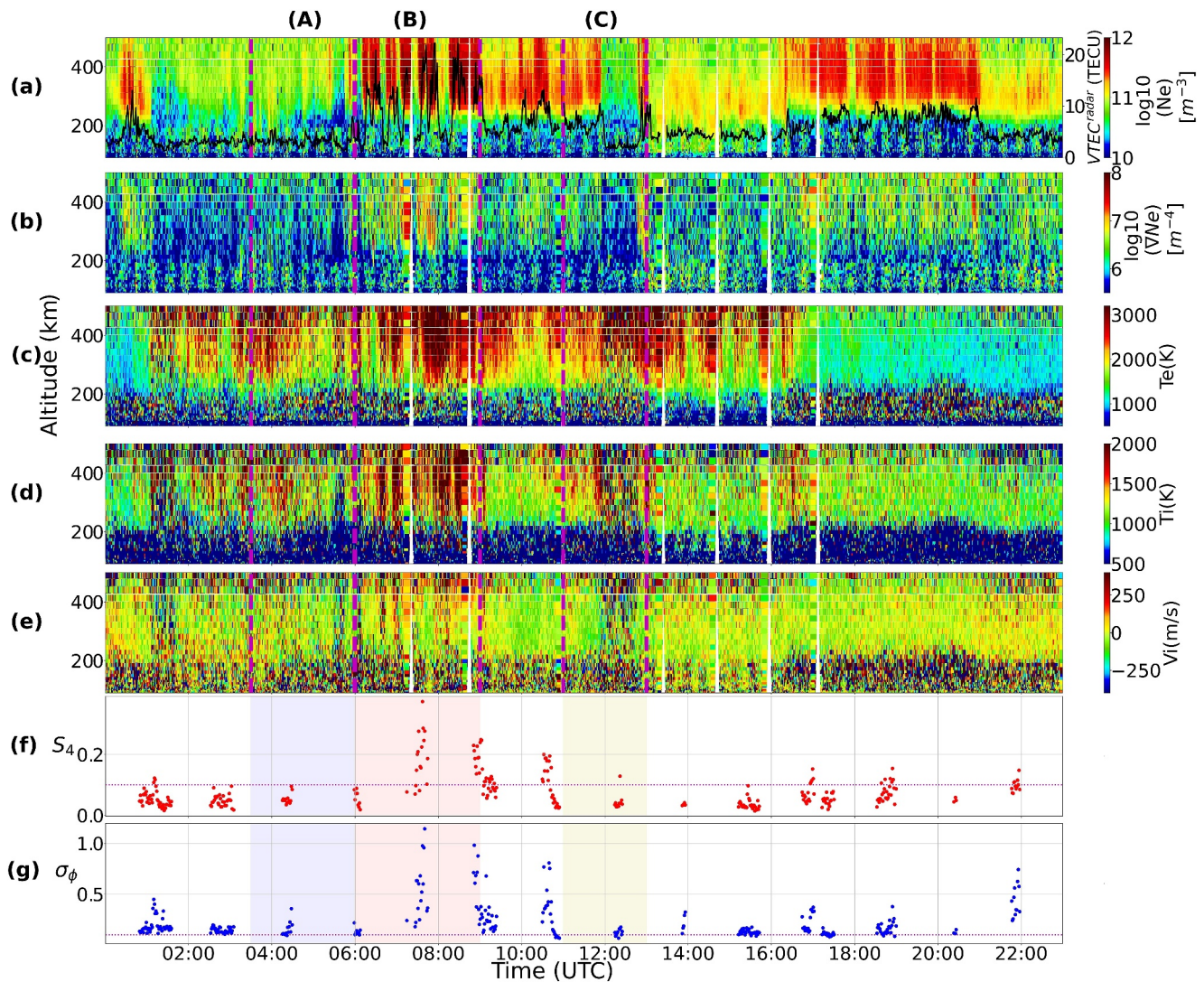


**Figure 6.** The field-aligned measurements from the ESR-42 m displaying the height profiles of  $N_e$  (panel a), gradients in density ( $\nabla N_e$ ) in panel (b),  $T_e$  (panel c),  $T_i$  (panel d) and  $V_i$  (panel e). Panels (f), (g) contain the  $S_4, \sigma_\phi$  values when conjunctions were present between the ESR-42 m beams and GNSS radio signals. The three intervals are separated using dashed vertical magenta lines in panels (a–e) and shaded in panels (f–g).

were conjunctions between the radar and GNSS beams. On comparing intervals (A), (B), (C) we clearly observe gradients associated with large density structures that are co-located with regions of enhanced  $T_e$  and  $T_i$  during interval (B). Elevated electron temperatures near regions of enhanced densities at F region altitudes indicate ongoing soft particle precipitation (Doe et al., 2001; Kersley et al., 1988; Vonrat-Reberac et al., 2001) whereas enhanced  $T_i$  indicate Joule heating of the ions (St.-Maurice & Hanson, 1982). The  $S_4$  and  $\sigma_\phi$  values are significantly enhanced from the background level during this interval. Together with Figure 5 this confirms the presence of irregularities from Fresnel to large-scales with sufficient strengths to perturb both the amplitude and phase of GNSS signals. These results are in line with the observations in Mitchell et al. (2005), Kintner et al. (2007), Jenner et al. (2020), Madhanakumar et al. (2024) where the authors associated scintillation occurrence to the presence of gradients in density structures. Notably, the vertical TEC observed by the radar closely matched the GNSS VTEC values observed in Figures 2 and 3.

A necessary condition for the production of irregularities is the existence of sources of free energy. Multiple mechanisms can then structure the plasma to produce scintillation causing irregularities in the high latitude ionosphere. Sheared plasma flow perpendicular to magnetic field can give rise to Kelvin-Helmholtz instability

(KHI), generating medium and large-scale irregularities (Basu et al., 1988; Keskinen et al., 1988; Oksavik et al., 2011). An increased plasma flow in the direction of density gradients can then efficiently generate smaller scale irregularities through Gradient-Drift instability (GDI) (Burston et al., 2009; Carlson et al., 2007, 2008; Tsunoda, 1988; Weber et al., 1984) such as in the trailing edges of polar cap patches. Spicher et al. (2020) had shown KHI to be an effective mechanism in generating density irregularities within minutes. GDI could then efficiently operate on these intermediate scale structures generating small-scale irregularities within tens of seconds (Carlson et al., 2007; Oksavik et al., 2012; J. Moen et al., 2012; Spicher et al., 2015). In addition to KHI, particle precipitation is also suggested to be the source of large-scale irregularities which can be further structured down to small-scales by GDI (Goodwin et al., 2015; Kelley et al., 1982; Oksavik et al., 2006, 2012). Roble and Rees (1977), Valladares et al. (1994) have shown that density variations of the order of 20% – 30% in the F region can be achieved within 15–20 min. Assuming a production rate of ionization at F region altitude to be  $\sim 8 \times 10^8 \text{ m}^{-3}\text{s}^{-1}$  from Millward et al. (1999)'s precipitation model, Hosokawa et al. (2016) estimated that the electron density in poleward moving auroral forms (PMAFs) increases by  $2 - 3 \times 10^{11} \text{ m}^{-3}$  within 5 min. Given a high density structure such as polar cap patches, KHI or soft precipitation can therefore structure the dense plasma producing large to intermediate scale irregularities within minutes which can then cascade into Fresnel scale structures that can cause simultaneous amplitude and phase scintillation in GNSS signals. Ivarsen et al. (2023), on the other hand, had found that the energy flux of precipitating particles decreases or remains unchanged with increasing geomagnetic activity whereas ionospheric irregularities and the associated phase scintillation increases significantly. The authors therefore suggested that other sources played a major role in producing irregularities associated with GNSS phase scintillation rather than soft precipitation during disturbed conditions.

We now proceed to place our scintillation observations on the 7<sup>th</sup> of November 2013 within the context of the aforementioned different mechanisms/processes. Referring back to interval (B) in Figures 2–4, we observed scintillation (predominantly in phase) even at lower latitudes as plasma structures of enhanced density entered the auroral oval. Furthermore, scintillation was present along the sides and inside these density enhancements indicating that they were already structured and had irregularities throughout. Similar observations of the presence of irregularities at both the edges and/or throughout regions of enhanced plasma density such as polar cap patches were also made by Gondarenko et al. (2003), Gondarenko and Guzdar (2004), Coker et al. (2004), Thayyil et al. (2021) and references therein. Interval (B) in Figures 5 and 6 show scintillation to be associated with dense plasma structures and in regions of enhanced  $T_i$  (or fast flows). This can provide the necessary conditions for KHI to evolve and grow. Similar to Carlson et al. (2007), the growth time of KHI was estimated using the maximized growth time equation:

$$\tau_{KHI} = \frac{5L}{V} \quad (3)$$

Using a velocity difference (V) of 300 m/s (from SuperDARN) and assuming a velocity difference scale length (L) of 10 km, similar to Carlson et al. (2007), the growth time of KHI was estimated to be about 3 min. In addition, ongoing soft particle precipitation was also observed during this interval. With an average convection velocity ranging between 400 and 700 m/s, as measured by SuperDARN, and assuming a latitudinal width of 3° for the auroral oval it would take approximately 7–10 min for the patches to transit across the auroral oval to the polar cap. If we assume an F region ionization production rate of  $\sim 8 \times 10^8 \text{ m}^{-3}\text{s}^{-1}$  from Millward et al. (1999), an estimated density increase of the order of  $1.5 - 2.5 \times 10^{11} \text{ el/m}^3$  can occur within 3–5 min. This suggests that plasma pre-structuring can be achieved by soft precipitation within minutes when patches are inside the auroral oval. With a larger precipitating flux, the plasma structuring can occur even faster. Furthermore, the presence of strong gradients associated with the density structures, as seen in Figure 6b, suggests that GDI could be active during this interval. The growth time for GDI in the linear regime can be calculated when  $\mathbf{k} \cdot \mathbf{B} = 0$ , as (Tsunoda, 1988):

$$\tau_{GDI} = \frac{L}{v_0} \quad (4)$$

with the gradient length scale, L, given as:

$$L = \frac{N_0}{\Delta N_e / \Delta x} \quad (5)$$

Here,  $v_0$  is the relative velocity of the plasma with respect to the neutrals,  $\Delta N_e / \Delta x$  the density gradients and  $N_0$  the background density. Using gradient and background density information from Figure (6) along with the plasma velocity from SuperDARN, GDI was estimated to grow as fast as 35 s using Equation 4. For the calculation, velocity of the neutral gas was ignored similar to J. Moen et al. (2012), Oksavik et al. (2012), Spicher et al. (2015).

We now proceed to provide a likely scenario of irregularity generation based on our observations of scintillation and the above discussed sources/instability mechanisms. Figures 2–6 reveal that the strongest scintillation occurred when large densities and gradients were present in regions of strong flows and particle precipitation. This suggests that TOIs and (or) polar cap patches provided the necessary large background density with KHI and soft particle precipitation structuring the plasma as the patches convected poleward. The enhancement in the phase scintillation could then be associated with the generation of large to intermediate scale sized irregularities within minutes as a result of fast flows and hence KHI as in Spicher et al. (2020) or to irregularity structuring by particle precipitation as in Kinrade et al. (2012), Makarevich et al. (2021), Oksavik et al. (2015). GDI could have further operated to produce the small-scale irregularities within seconds resulting in simultaneous amplitude scintillation in GNSS frequencies. It is worth pointing out that we are only able to provide estimates for the growth times of the different processes/instabilities due to our assumptions and uncertainties associated with different parameters used in Equations 3–5. Nevertheless, the estimates suggest that our observations of intense amplitude and phase scintillation, and hence the presence of irregularities of varying scale-sizes, are consistent with different irregularity generation mechanisms/processes. We however emphasize the need to conduct more studies to understand the effectiveness of different sources/instability mechanisms and their relative importance in generating a spectrum of irregularities that can simultaneously affect both the amplitude and phase of GNSS signals in the polar ionosphere.

### 5.3. Interval (C)

During interval (C), the ESR-32 m field-of-view in the post-noon sector was covered by ionospheric plasma of depleted density as compared to interval (B) and similar to interval (A). Below we briefly discuss the formation process of this depletion region that led to the significant removal of scintillation in GNSS signals. Referring to Figure 1a, this interval corresponds to the period when IMF  $B_y$  turned from being positive to strongly negative whereas  $B_z$  turned northward after being strongly southward. A closer look at the time history of the TEC maps (see Movie S1) during this interval shows a TOI being cut to form a patch that propagated poleward just before the depletion region covered the polar cap ionosphere. The detachment was similar to the one observed in Milan et al. (2002) and occurred when the plasma flow alternated between poleward and zonal directions near the cusp region as a result of  $B_y$  reversal, changing the entry point of the plasma into the high latitude polar cap (Rodger et al., 1994). Valladares et al. (1994) observed fast plasma jets with velocities exceeding 2,000 m/s and  $T_i$  in excess of 5,000 K in the pre-noon sector during IMF  $B_y$  negative conditions. As the region of plasma jets were co-located with regions of low F region densities, the authors suggested the enhanced recombination rate of  $O^+ + N_2$  reaction as the decisive factor that led to the depletion in the electron density. However, in our study the ion velocities, as measured by SuperDARN, rarely exceeded 700 m/s during interval (C). Furthermore, comparing the ESR-32 m scans of  $T_i$  in Figure 5c during intervals (B) and (C), we observe similar regions of ion frictional heating but density was severely depleted only during interval (C) suggesting that Joule heating alone cannot account for the significant density depletion observed across the radar field-of-view in line with the observations in Milan et al. (2002). Similar conclusions were reached by Ren et al. (2020) as well after the authors compared their observed density depletion in the Sondrestrom ISR to the estimated decrease due to Joule heating. The authors suggested that ion frictional heating could not account for the observed depletion region above 300 km in the ISR scans as well as in their TEC maps. As an alternate solution, the transport of low density structures from the dawn or dusk sector, depending on the sign of IMF  $B_y$ , was offered to explain the formation of the density depletion in the cusp/polar cap regions (Milan et al., 2002; Ren et al., 2020). In fact, the time evolution of TEC across the polar ionosphere between 11:00 - 13:00 UTC (see Movie S1) revealed a depleted region of TEC being drawn into the post-noon cusp/polar cap from the westward-directed return flow channel in the dawn sector during negative  $B_y$  conditions. We therefore conclude that the transport of this low density plasma played a

dominant role in the erosion of irregularities in the post-noon sector leading to the significant weakening of amplitude and phase scintillation in GNSS signals.

To summarize, a comparison of scintillation strengths during intervals (B) and (C) in Figures 1e and 1f revealed that the most intense period of scintillation occurred during interval (B), that is, in the pre-noon sector. Observations from the ESR (both 32 and 42 m) in Figures 5 and 6 show that the most striking differences between the two intervals are in the electron densities and gradients. Even though both electron and ion temperatures during interval (C) appear to be noisy, due to low density for radar back-scatter, enhanced regions of  $T_e$  and  $T_i$  were still present though with reduced intensity as compared to interval (B). Together with Figure 6a, which shows a depleted region of ionospheric plasma with low  $VTEC^{radar}$  between 12:00 - 13:00 UTC, Figure 6b shows that the ionosphere, during interval (C), was devoid of significant density gradients when compared to interval (B). The notable reduction in the strength of amplitude scintillation during interval (C) then suggests that fast flows (resulting in enhanced  $T_i$ ) and ongoing soft precipitation become less effective in creating Fresnel sized irregularities when regions of dense plasma are absent.

## 6. Conclusion

We have presented a multiscale study of GNSS scintillation in the dayside polar ionosphere using a suite of both ground-based and space borne instruments during non-storm conditions. The different evolutionary stages of both amplitude and phase scintillation, from a state of low disturbance to intensification followed by the reduction in strength, were investigated in detail and the observations were placed in relation to the changes in the IMF  $B_y$ ,  $B_z$  components. Additionally, attempts were made to understand the role of different instability mechanisms in the high latitude ionosphere that could help generate irregularities of various scale-sizes capable of inducing simultaneous amplitude and phase scintillation in GNSS signals. The key observations and interpretations of this study are summarized below.

1. Intense amplitude and phase scintillation, lasting for  $\sim 1$  hour, were observed in the pre-noon sector during non-storm conditions with the 1-s  $S_4$  reaching a maximum value of 0.75 whereas  $\sigma_\phi$  reached values up to 2.2 rad.
2. Fresnel scale irregularities were observed both in the auroral oval as well as inside the polar cap with the source being high density structures transported from subauroral latitudes. Associated amplitude scintillation in both the regions exhibited similar strengths suggesting that Fresnel structures maintained significant power regardless of being located in regions with auroral dynamics or not.
3. The convecting dense structures intersected regions of strong ion heating (i.e., enhanced flows) and structured soft particle precipitation, and were observed to be associated with significant density gradients.
4. The northward turning of the IMF  $B_z$  component together with the strong negative excursion of the  $B_y$  component resulted in the westward transport of a region of depleted density into the post-noon sector from the dawn sector. This led to the erosion of Fresnel and large-scale sized irregularities resulting in the significant weakening of amplitude and phase scintillation in the post-noon sector.

Our observations and results complement the existing literature where intense amplitude scintillation were frequently observed to occur during severe geomagnetic conditions and in the post-noon sector, with large densities playing a crucial role in the occurrence and strength of scintillation in GNSS signals. The findings presented here suggest that geomagnetic conditions cannot always capture the true ionospheric response on radio signals such as that from GNSS, making scintillation forecasting solely based on geomagnetic activity difficult. Furthermore, we emphasize that the plasma intake from lower latitudes in the pre-noon sector can be equally important as that from the post-noon sector for scintillation studies. In addition, even though post-noon sector is an excellent breeding ground for intense irregularities of different scale-sizes that can significantly perturb GNSS signals, the IMF  $B_y$  and  $B_z$  components can help in the transport of low density plasma thereby removing/significantly reducing scintillation. Further work has to be done to reveal how often the reversals in IMF components during non-storm conditions lead to plasma depletion in the post-noon sector and its subsequent effect on scintillation in GNSS signals.

Appendix A: Overview of Instruments/Data Sources

Table A1

Overview of the Instruments/Data Sources, Measurement Quantities As Well As Their Coverage Used in the Study

Data source/instrument	Latitude	Longitude	Measurement
EISCAT 32 m (ESR-32 m)	78.15°	16.02°	$N_e, T_e, T_i, V_i$
EISCAT 42 m (ESR-42 m)	78.15°	16.02°	$N_e, T_e, T_i, V_i$
NovAtel GPStation-6 GISTM	78.1° (KHO), 74.5° (BJN), 78.9° (NYA)	16.0° (KHO), 19.0° (BJN), 11.9° (NYA)	$S_4, \sigma_\phi, VTEC, ROT$
CEDAR Madrigal	60° – 90°	0° – 360°	VTEC
SuperDARN	60° – 90°	0° – 360°	Convection velocity, electric potential
DMSP SSUSI	60° – 90°	0° – 360°	Poleward, equatorward auroral boundaries
OMNI	N/A	N/A	$B_x, B_y, B_z$ , flow speed, pressure, proton density
World Data Center for Geomagnetism	(–34°) – 48°	2° – 293°	SYMH
World Data Center for Geomagnetism	56.5° – 78°	(–157°) – 171°	AL, AU, AE

Appendix B: 1-s  $S_4$  and  $\sigma_\phi$  Indices

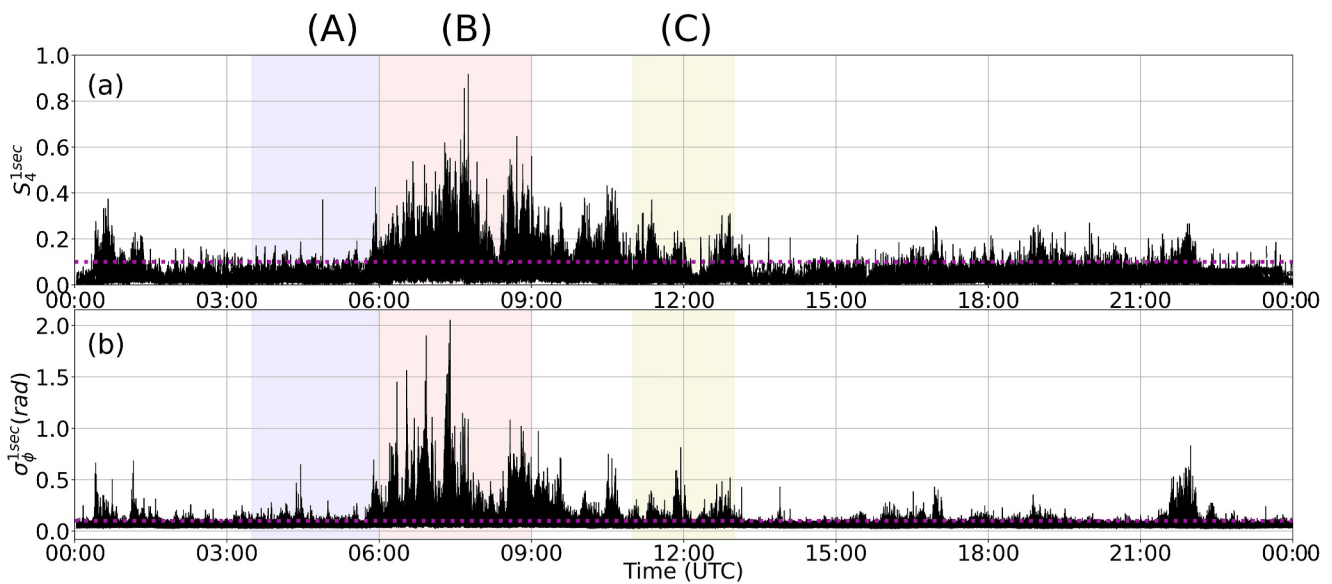


Figure B1.  $S_4$  (panel a),  $\sigma_\phi$  (panel b) indices with a resolution of 1-s on 07 November 2013. Data from all available PRNs of different GNSS constellations have been included. A magenta dotted horizontal line, in both panels, show the threshold of 0.1 used to distinguish between scintillation and non-scintillation events.

Data Availability Statement

Data from EISCAT can be obtained from the Madrigal database (Hägström, 2013). The GNSS data from KHO, NYA and BJN can be obtained from the University of Bergen Global Navigation Satellite System Data Collection (Oksavik, 2020b). The TEC data used in TEC maps are accessible from the Madrigal database (Coster, 2013). Raw SuperDARN data with DOI's can be accessed via SuperDARN data collection (SuperDARN, 2021). Processing to higher level products is done using the Radar Software Toolkit (SuperDARN Data Analysis Working



**Acknowledgments**

This research is part of the CASCADE project funded by the Research Council of Norway (RCN) Grant 326039. UiT the Arctic University of Norway's contribution to the EISCAT\_3D project funded by RCN through research infrastructure Grant 245683 is acknowledged. MM would like to thank Radovan Bast from the High Performance Computing (HPC) group of UiT for valuable discussions on enhancing computational speed and performance of scripts on a server. EISCAT is an international association supported by research organizations in China (CRIRP), Finland (SA), Japan (NIPR and ISEE), Norway (NFR), Sweden (VR), and the United Kingdom (UKRI). The authors acknowledge the use of SuperDARN data. SuperDARN is a collection of radars funded by national scientific funding agencies of Australia, Canada, China, France, Italy, Japan, Norway, South Africa, United Kingdom and the United States of America. AJC acknowledges support from NSF award AGS1726377, NASA awards 80NSSC20K1785, 80NSSC23M0193 and ONR award N00014-24-1-2122. GPS TEC data products and access through the Madrigal distributed data system are provided to the community (<http://www.openmadrigal.org>) by the Massachusetts Institute of Technology (MIT) under support from US National Science Foundation Grant AGS-1952737. Data for the TEC processing is provided from the following organizations: UNAVCO, Scripps Orbit and Permanent Array Center, Institut Geographique National, France, International GNSS Service, The Crustal Dynamics Data Information System (CDDIS), National Geodetic Survey, Instituto Brasileiro de Geografia e Estatística, RAMSAC CORS of Instituto Geográfico Nacional de la República Argentina, Arcébio Observatory, Low-Latitude Ionospheric Sensor Network (LISN), Topcon Positioning Systems, Inc., Canadian High Arctic Ionospheric Network, Institute of Geology and Geophysics, Chinese Academy of Sciences, China Meteorology Administration, Centro di Ricerche Sismologiche, Système d'Observation du Niveau des Eaux Littorales (SONEL), RENAG: REseau NAtional GPS permanent, GeoNet—the official source of geological hazard information for New Zealand, GNSS Reference Networks, Finnish Meteorological Institute, SWEPOS—Sweden, Hartebeesthoek Radio Astronomy Observatory, Crustal Dynamics Data Information System (CDDIS), Astronomical Institute of the University of Bern, TrigNet Web Application, South Africa, Australian Space Weather Services, RETE INTEGRATA NAZIONALE GPS, Estonian Land Board, and Virginia Tech Center for Space Science and Engineering Research. The IMF and solar wind data

Group, 2022). Data for the IMF components, solar wind, SYMH and the auroral electrojet indices can be obtained from OMNI database (King & Papitashvili, 2013). The auroral boundary data is obtained from the DMSP SSUSI instrument (Paxton, 2013).

**References**

Alfonsi, L., Spogli, L., De Franceschi, G., Romano, V., Aquino, M., Dodson, A., & Mitchell, C. N. (2011). Bipolar climatology of GPS ionospheric scintillation at solar minimum. *Radio Science*, 46(3), RS0D05. <https://doi.org/10.1029/2010RS004571>

Basu, S., Basu, S., MacKenzie, E., Coley, W. R., Sharber, J. R., & Hoegy, W. R. (1990). Plasma structuring by the gradient drift instability at high latitudes and comparison with velocity shear driven processes. *Journal of Geophysical Research*, 95(A6), 7799–7818. <https://doi.org/10.1029/JA095iA06p07799>

Basu, S., Basu, S., MacKenzie, E., Fougere, P. F., Coley, W. R., Maynard, N. C., et al. (1988). Simultaneous density and electric field fluctuation spectra associated with velocity shears in the auroral oval. *Journal of Geophysical Research*, 93(A1), 115–136. <https://doi.org/10.1029/JA093iA01p0115>

Burrell, A., van der Meeren, C., & Laundal, K. M. (2020). aburrell/aacgm2: Version 2.6.0. *Zenodo*. <https://doi.org/10.5281/zenodo.3598705>

Burston, R., Astin, I., Mitchell, C., Alfonsi, L., Pedersen, T., & Skone, S. (2009). Correlation between scintillation indices and gradient drift wave amplitudes in the northern polar ionosphere. *Journal of Geophysical Research*, 114(A7), A07309. <https://doi.org/10.1029/2009JA014151>

Cardenas-O'Toole, A. M., Zou, S., Ren, J., Wang, Z., & Jayachandran, P. T. (2024). Phase and amplitude scintillations associated with polar cap patches: Statistical and event analyses. *Journal of Geophysical Research: Space Physics*, 129(4), e2023JA031765. <https://doi.org/10.1029/2023JA031765>

Carlson, H. C., Moen, J., Oksavik, K., Nielsen, C. P., McCrea, I. W., Pedersen, T. R., & Gallop, P. (2006). Direct observations of injection events of subauroral plasma into the polar cap. *Geophysical Research Letters*, 33(5), L05103. <https://doi.org/10.1029/2005GL025230>

Carlson, H. C., Oksavik, K., & Moen, J. (2008). On a new process for cusp irregularity production. *Annales Geophysicae*, 26(9), 2871–2885. <https://doi.org/10.5194/angeo-26-2871-2008>

Carlson, H. C., Oksavik, K., Moen, J., van Eyken, A. P., & Guio, P. (2002). ESR mapping of polar-cap patches in the dark cusp. *Geophysical Research Letters*, 29(10), 24-1–24-4. <https://doi.org/10.1029/2001GL014087>

Carlson, H. C., Pedersen, T., Basu, S., Keskinen, M., & Moen, J. (2007). Case for a new process, not mechanism, for cusp irregularity production. *Journal of Geophysical Research*, 112(A11), A11304. <https://doi.org/10.1029/2007JA012384>

Carrano, C., Groves, K., McNeil, W., & Doherty, P. (2013). Direct measurement of the residual in the ionosphere-free linear combination during scintillation. In *Proceedings of the 2013 international technical meeting of the Institute of navigation* (pp. 585–596).

Chisham, G., Lester, M., Milan, S. E., Freeman, M. P., Bristow, W. A., Grocott, A., et al. (2007). A decade of the super dual auroral radar network (SUPERDARN): Scientific achievements, new techniques and future directions. *Surveys in Geophysics*, 28(1), 33–109. <https://doi.org/10.1007/s10712-007-9017-8>

Coker, C., Bust, G. S., Doe, R. A., & Gaussiran, T. L. (2004). High-latitude plasma structure and scintillation. *Radio Science*, 39(1), 1–10. <https://doi.org/10.1029/2002RS002833>

Coster, A. (2013). Data from the cedar madrigal database. *MIT/Haystack Observatory*. Retrieved from [https://w3id.org/cedar?experiment\\_list=experiments3/2013/gps/07nov13&file\\_list=gps131107g.004.hdf5](https://w3id.org/cedar?experiment_list=experiments3/2013/gps/07nov13&file_list=gps131107g.004.hdf5)

Cowley, S. W. H., & Lockwood, M. (1992). Excitation and decay of solar wind-driven flows in the magnetosphere-ionosphere system. *Annales Geophysicae*, 10(1–2), 103–115.

Crowley, G., Ridley, A. J., Deist, D., Wing, S., Knipp, D. J., Emery, B. A., et al. (2000). Transformation of high-latitude ionospheric f region patches into blobs during the March 21, 1990, storm. *Journal of Geophysical Research*, 105(A3), 5215–5230. <https://doi.org/10.1029/1999JA900357>

D'Angelo, G., Piersanti, M., Pignalberi, A., Coco, I., De Michelis, P., Tozzi, R., et al. (2021). Investigation of the physical processes involved in GNSS amplitude scintillations at high latitude: A case study. *Remote Sensing*, 13(13), 2493. <https://doi.org/10.3390/rs13132493>

De Franceschi, G., Alfonsi, L., Romano, V., Aquino, M., Dodson, A., Mitchell, C. N., et al. (2008). Dynamics of high-latitude patches and associated small-scale irregularities during the October and November 2003 storms. *Journal of Atmospheric and Solar-Terrestrial Physics*, 70(6), 879–888. <https://doi.org/10.1016/j.jastp.2007.05.018>

Doe, R. A., Kelly, J. D., & Sánchez, E. R. (2001). Observations of persistent dayside F region electron temperature enhancements associated with soft magnetosheathlike precipitation. *Journal of Geophysical Research*, 106(A3), 3615–3630. <https://doi.org/10.1029/2000JA000186>

Faehn Follestad, A., Herlingshaw, K., Ghadjar, H., Knudsen, D. J., McWilliams, K. A., Moen, J. I., et al. (2020). Dayside field-aligned current impacts on ionospheric irregularities. *Geophysical Research Letters*, 47(11), e2019GL086722. <https://doi.org/10.1029/2019GL086722>

Forte, B., Coleman, C., Skone, S., Häggström, I., Mitchell, C., Da Dalt, F., et al. (2017). Identification of scintillation signatures on GPS signals originating from plasma structures detected with EISCAT incoherent scatter radar along the same line of sight. *Journal of Geophysical Research: Space Physics*, 122(1), 916–931. <https://doi.org/10.1002/2016JA023271>

Forte, B., & Radicella, S. M. (2002). Problems in data treatment for ionospheric scintillation measurements. *Radio Science*, 37(6), 8-1–8-5. <https://doi.org/10.1029/2001RS002508>

Fremouw, E. J., Leadabrand, R. L., Livingston, R. C., Cousins, M. D., Rino, C. L., Fair, B. C., & Long, R. A. (1978). Early results from the dna wideband satellite experiment—Complex-signal scintillation. *Radio Science*, 13(1), 167–187. <https://doi.org/10.1029/RS013i001p0167>

Gondarenko, N. A., & Guzdar, P. N. (2004). Plasma patch structuring by the nonlinear evolution of the gradient drift instability in the high-latitude ionosphere. *Journal of Geophysical Research*, 109(A9), A09301. <https://doi.org/10.1029/2004JA010504>

Gondarenko, N. A., Guzdar, P. N., Sojka, J. J., & David, M. (2003). Structuring of high latitude plasma patches with variable drive. *Geophysical Research Letters*, 30(4), 1165. <https://doi.org/10.1029/2002GL016437>

Gonzalez, W. D., Joselyn, J. A., Kamide, Y., Kroehl, H. W., Rostoker, G., Tsurutani, B. T., & Vasyliunas, V. M. (1994). What is a geomagnetic storm? *Journal of Geophysical Research*, 99(A4), 5771–5792. <https://doi.org/10.1029/93JA02867>

Goodwin, L. V., Isernhien, B., Miles, D. M., Patra, S., van der Meeren, C., Buchert, S. C., et al. (2015). Swarm in situ observations of f region polar cap patches created by cusp precipitation. *Geophysical Research Letters*, 42(4), 996–1003. <https://doi.org/10.1002/2014GL026210>

Häggström, I. (2013). Data from the cedar madrigal database. *EISCAT Scientific Association*. Retrieved from [https://w3id.org/cedar?experiment\\_list=experiments/2013/lyr/07nov13&file\\_list=MAD6400\\_2013-11-07\\_folke\\_32%32ma.hdf5](https://w3id.org/cedar?experiment_list=experiments/2013/lyr/07nov13&file_list=MAD6400_2013-11-07_folke_32%32ma.hdf5)

Horvath, I., & Crozier, S. (2007). Software developed for obtaining GPS-derived total electron content values. *Radio Science*, 42(2), RS2002. <https://doi.org/10.1029/2006RS003452>

are provided by the NASA OMNIWeb service. The SYMH and the AE indices (AL, AU, AE) used in this paper were provided by the WDC for Geomagnetism, Kyoto (<http://wdc.kugi.kyoto-u.ac.jp/wdc/Sec3.html>). The DMSP SSUSI data were obtained from The Johns Hopkins University Applied Research Laboratory.

- Hosokawa, K., Taguchi, S., & Ogawa, Y. (2016). Periodic creation of polar cap patches from auroral transients in the cusp. *Journal of Geophysical Research: Space Physics*, 121(6), 5639–5652. <https://doi.org/10.1002/2015JA022221>
- Hutchinson, J. A., Wright, D. M., & Milan, S. E. (2011). Geomagnetic storms over the last solar cycle: A superposed epoch analysis. *Journal of Geophysical Research*, 116(A9), A09211. <https://doi.org/10.1029/2011JA016463>
- Ivarsen, M. F., Jin, Y., Spicher, A., St-Maurice, J.-P., Park, J., & Billett, D. (2023). GNSS scintillations in the cusp, and the role of precipitating particle energy fluxes. *Journal of Geophysical Research: Space Physics*, 128(10), e2023JA031849. <https://doi.org/10.1029/2023JA031849>
- Jenner, L. A., Wood, A. G., Dorrian, G. D., Oksavik, K., Yeoman, T. K., Fogg, A. R., & Coster, A. J. (2020). Plasma density gradients at the edge of polar ionospheric holes: The absence of phase scintillation. *Annales Geophysicae*, 38(2), 575–590. <https://doi.org/10.5194/angeo-38-575-2020>
- Jiao, Y., & Morton, Y. T. (2015). Comparison of the effect of high-latitude and equatorial ionospheric scintillation on GPS signals during the maximum of solar cycle 24. *Radio Science*, 50(9), 886–903. <https://doi.org/10.1002/2015RS005719>
- Jiao, Y., Morton, Y. T., Taylor, S., & Pelgrum, W. (2013). Characterization of high-latitude ionospheric scintillation of GPS signals. *Radio Science*, 48(6), 698–708. <https://doi.org/10.1002/2013RS005259>
- Jin, Y., Moen, J. I., & Miloch, W. J. (2014). Gps scintillation effects associated with polar cap patches and substorm auroral activity: Direct comparison. *Journal of Space Weather and Space Climate*, 4, A23. <https://doi.org/10.1051/swsc/2014019>
- Jin, Y., Moen, J. I., & Miloch, W. J. (2015). On the collocation of the cusp aurora and the GPS phase scintillation: A statistical study. *Journal of Geophysical Research: Space Physics*, 120(10), 9176–9191. <https://doi.org/10.1002/2015JA021449>
- Jin, Y., Moen, J. I., Oksavik, K., Spicher, A., Clausen, L. B., & Miloch, W. J. (2017). GPS scintillations associated with cusp dynamics and polar cap patches. *Journal of Space Weather and Space Climate*, 7, A23. <https://doi.org/10.1051/swsc/2017022>
- Jin, Y., & Oksavik, K. (2018). Gps scintillations and losses of signal lock at high latitudes during the 2015 st. Patrick's day storm. *Journal of Geophysical Research: Space Physics*, 123(9), 7943–7957. <https://doi.org/10.1029/2018JA025933>
- Kelley, M. C., Vickrey, J. F., Carlson, C. W., & Torbert, R. (1982). On the origin and spatial extent of high-latitude f region irregularities. *Journal of Geophysical Research*, 87(A6), 4469–4475. <https://doi.org/10.1029/JA087iA06p04469>
- Kersley, L., Pryse, S., & Wheadon, N. (1988). Small scale ionospheric irregularities near regions of soft particle precipitation: Scintillation and eiscat observations. *Journal of Atmospheric and Terrestrial Physics*, 50(12), 1047–1055. [https://doi.org/10.1016/0021-9169\(88\)90094-3](https://doi.org/10.1016/0021-9169(88)90094-3)
- Keskinen, M. J., Mitchell, H. G., Fedder, J. A., Satyanarayana, P., Zalesak, S. T., & Huba, J. D. (1988). Nonlinear evolution of the Kelvin-Helmholtz instability in the high-latitude ionosphere. *Journal of Geophysical Research*, 93(A1), 137–152. <https://doi.org/10.1029/JA093iA01p00137>
- King, J. H., & Papitashvili, N. E. (2005). Solar wind spatial scales in and comparisons of hourly wind and ace plasma and magnetic field data. *Journal of Geophysical Research*, 110(A2), A02104. <https://doi.org/10.1029/2004JA010649>
- King, J. H., & Papitashvili, N. E. (2013). OMNI combined, definitive, 1-minute IMF and plasma data time-shifted to the nose of the earth's bow shock, plus magnetic indices. *AdnetSystems, NASA GSFC*. Retrieved from <https://cdaweb.gsfc.nasa.gov/>
- Kinrade, J., Mitchell, C. N., Yin, P., Smith, N., Jarvis, M. J., Maxfield, D. J., et al. (2012). Ionospheric scintillation over Antarctica during the storm of 5–6 April 2010. *Journal of Geophysical Research*, 117(A5), A05304. <https://doi.org/10.1029/2011JA017073>
- Kintner, P. M., Kil, H., Beach, T. L., & de Paula, E. R. (2001). Fading timescales associated with GPS signals and potential consequences. *Radio Science*, 36(4), 731–743. <https://doi.org/10.1029/1999RS002310>
- Kintner, P. M., Ledvina, B. M., & de Paula, E. R. (2007). GPS and ionospheric scintillations. *Space Weather*, 5(9), S09003. <https://doi.org/10.1029/2006SW000260>
- Lehtinen, M. S., & Huuskonen, A. (1996). General incoherent scatter analysis and guidap. *Journal of Atmospheric and Terrestrial Physics*, 58(1), 435–452. [https://doi.org/10.1016/0021-9169\(95\)00047-X](https://doi.org/10.1016/0021-9169(95)00047-X)
- Liu, Y., Fu, L., Wang, J., & Zhang, C. (2017). Study of gnss loss of lock characteristics under ionosphere scintillation with GNSS data at WEIPA (Australia) during solar maximum phase. *Sensors*, 17(10), 2205. <https://doi.org/10.3390/s17102205>
- Madhanakumar, M., Kashcheyev, A., & Jayachandran, P. T. (2022). On the dependence of amplitude and phase scintillation indices on magnetic field aligned angle: A statistical investigation at high latitudes. *IEEE Geoscience and Remote Sensing Letters*, 19, 1–5. <https://doi.org/10.1109/LGRS.2021.3115668>
- Madhanakumar, M., Spicher, A., Vierinen, J., & Oksavik, K. (2024). On the strength of E and F region irregularities for GNSS scintillation in the dayside polar ionosphere. *Journal of Atmospheric and Solar-Terrestrial Physics*, 256, 106197. <https://doi.org/10.1016/j.jastp.2024.106197>
- Makarevich, R. A., Crowley, G., Azeem, I., Ngwira, C., & Forsythe, V. V. (2021). Auroral E-region as a source region for ionospheric scintillation. *Journal of Geophysical Research: Space Physics*, 126(5), e2021JA029212. <https://doi.org/10.1029/2021JA029212>
- McCaffrey, A. M., & Jayachandran, P. (2019). Determination of the refractive contribution to GPS phase scintillation. *Journal of Geophysical Research: Space Physics*, 124(2), 1454–1469. <https://doi.org/10.1029/2018JA025759>
- Meziane, K., Kashcheyev, A., Patra, S., Jayachandran, P. T., & Hamza, A. M. (2020). Solar cycle variations of GPS amplitude scintillation for the polar region. *Space Weather*, 18(8), e2019SW002434. <https://doi.org/10.1029/2019SW002434>
- Milan, S. E., Lester, M., & Yeoman, T. K. (2002). HF radar polar patch formation revisited: Summer and winter variations in dayside plasma structuring. *Annales Geophysicae*, 20(4), 487–499. <https://doi.org/10.5194/angeo-20-487-2002>
- Millward, G. H., Moffett, R. J., Balmforth, H. F., & Rodger, A. S. (1999). Modeling the ionospheric effects of ion and electron precipitation in the cusp. *Journal of Geophysical Research*, 104(A11), 24603–24612. <https://doi.org/10.1029/1999JA900249>
- Mitchell, C. N., Alfonsi, L., De Franceschi, G., Lester, M., Romano, V., & Wernik, A. W. (2005). GPS TEC and scintillation measurements from the polar ionosphere during the October 2003 storm. *Geophysical Research Letters*, 32(12), L12S03. <https://doi.org/10.1029/2004GL021644>
- Moen, J., Carlson, H. C., Oksavik, K., Nielsen, C. P., Pryse, S. E., Middleton, H. R., et al. (2006). Eiscat observations of plasma patches at sub-auroral cusp latitudes. *Annales Geophysicae*, 24(9), 2363–2374. <https://doi.org/10.5194/angeo-24-2363-2006>
- Moen, J., Oksavik, K., Abe, T., Lester, M., Saito, Y., Bekkeng, T. A., & Jacobsen, K. S. (2012). First in-situ measurements of HF radar echoing targets. *Geophysical Research Letters*, 39(7), L07104. <https://doi.org/10.1029/2012GL051407>
- Moen, J. I., Oksavik, K., Alfonsi, L., Daaball, Y., Romano, V., & Spogli, L. (2013). Space weather challenges of the polar cap ionosphere. *Journal of Space Weather and Space Climate*, 3, A02. <https://doi.org/10.1051/swsc/2013025>
- Nishimura, Y., Kelly, T., Jayachandran, P. T., Mrak, S., Semeter, J. L., Donovan, E. F., et al. (2023). Nightside high-latitude phase and amplitude scintillation during a substorm using 1-second scintillation indices. *Journal of Geophysical Research: Space Physics*, 128(8), e2023JA031402. <https://doi.org/10.1029/2023JA031402>
- Nishitani, N., Ruohoniemi, J. M., Lester, M., Baker, J. B. H., Koustov, A. V., Shepherd, S. G., et al. (2019). Review of the accomplishments of mid-latitude super dual auroral radar network (SUPERDARN) HF radars. *Progress in Earth and Planetary Science*, 6(1), 27. <https://doi.org/10.1186/s40645-019-0270-5>

- Oksavik, K. (2020a). Documentation of GNSS total electron content and scintillation data (60 s) at svalbard. *DataverseNO*. <https://doi.org/10.18710/EASBYX>
- Oksavik, K. (2020b). The university of bergen global navigation satellite system data collection, DataverseNO. *DataverseNO*. <https://doi.org/10.18710/AJ4S-X394>
- Oksavik, K., Moen, J., Lester, M., Bekkeng, T. A., & Bekkeng, J. K. (2012). In situ measurements of plasma irregularity growth in the cusp ionosphere. *Journal of Geophysical Research*, *117*(A11), A11301. <https://doi.org/10.1029/2012JA017835>
- Oksavik, K., Moen, J. I., Rekaa, E. H., Carlson, H. C., & Lester, M. (2011). Reversed flow events in the cusp ionosphere detected by superdarn HF radars. *Journal of Geophysical Research*, *116*(A12), A12303. <https://doi.org/10.1029/2011JA016788>
- Oksavik, K., Ruohoniemi, J. M., Greenwald, R. A., Baker, J. B. H., Moen, J., Carlson, H. C., et al. (2006). Observations of isolated polar cap patches by the European incoherent scatter (EISCAT) svalbard and super dual auroral radar network (SUPERDARN) Finland radars. *Journal of Geophysical Research*, *111*(A5), A05310. <https://doi.org/10.1029/2005JA011400>
- Oksavik, K., van der Meeren, C., Lorentzen, D. A., Baddeley, L. J., & Moen, J. (2015). Scintillation and loss of signal lock from poleward moving auroral forms in the cusp ionosphere. *Journal of Geophysical Research: Space Physics*, *120*(10), 9161–9175. <https://doi.org/10.1002/2015JA021528>
- Paxton, L. J. (2013). DMSP SSUSI data products. Retrieved from [https://ssusi.jhuapl.edu/data\\_products](https://ssusi.jhuapl.edu/data_products)
- Paxton, L. J., Meng, C.-I., Fountain, G. H., Ogorzalek, B. S., Darlington, E. H., Gary, S. A., et al. (1992). Special sensor ultraviolet spectrographic imager: An instrument description. *SPIE Proceedings*, *1745*, 2–15. <https://doi.org/10.1117/12.60595>
- Paxton, L. J., Morrison, D., Zhang, Y., Kil, H., Wolven, B., Ogorzalek, B. S., & Meng, C.-I. (2002). Validation of remote sensing products produced by the special sensor ultraviolet scanning imager (SSUSI). *a far UV-imaging spectrograph on DMSP F-16*, *4485*, 338–348. <https://doi.org/10.1117/12.454268>
- Prikryl, P., Jayachandran, P. T., Mushini, S. C., & Chadwick, R. (2011). Climatology of GPS phase scintillation and HF radar backscatter for the high-latitude ionosphere under solar minimum conditions. *Annales Geophysicae*, *29*(2), 377–392. <https://doi.org/10.5194/angeo-29-377-2011>
- Ren, J., Zou, S., Kendall, E., Coster, A., Sterne, K., & Ruohoniemi, M. (2020). Direct observations of a polar cap patch formation associated with dayside reconnection driven fast flow. *Journal of Geophysical Research: Space Physics*, *125*(4), e2019JA027745. <https://doi.org/10.1029/2019JA027745>
- Rideout, W., & Coster, A. (2006). Automated GPS processing for global total electron content data. *GPS Solutions*, *10*(3), 219–228. <https://doi.org/10.1007/s10291-006-0029-5>
- Roble, R., & Rees, M. (1977). Time-dependent studies of the aurora: Effects of particle precipitation on the dynamic morphology of ionospheric and atmospheric properties. *Planetary and Space Science*, *25*(11), 991–1010. [https://doi.org/10.1016/0032-0633\(77\)90146-5](https://doi.org/10.1016/0032-0633(77)90146-5)
- Rodger, A. S., Pinnock, M., Dudeney, J. R., Baker, K. B., & Greenwald, R. A. (1994). A new mechanism for polar patch formation. *Journal of Geophysical Research*, *99*(A4), 6425–6436. <https://doi.org/10.1029/93JA01501>
- Ruohoniemi, J. M., & Baker, K. B. (1998). Large-scale imaging of high-latitude convection with super dual auroral radar network HF radar observations. *Journal of Geophysical Research*, *103*(A9), 20797–20811. <https://doi.org/10.1029/98JA01288>
- Ruohoniemi, J. M., & Greenwald, R. A. (1996). Statistical patterns of high-latitude convection obtained from goose bay HF radar observations. *Journal of Geophysical Research*, *101*(A10), 21743–21763. <https://doi.org/10.1029/96JA01584>
- Semeter, J., Mrak, S., Hirsch, M., Swoboda, J., Akbari, H., Starr, G., et al. (2017). GPS signal corruption by the discrete aurora: Precise measurements from the mahali experiment. *Geophysical Research Letters*, *44*(19), 9539–9546. <https://doi.org/10.1002/2017GL073570>
- Shepherd, S. G. (2014). Altitude-adjusted corrected geomagnetic coordinates: Definition and functional approximations. *Journal of Geophysical Research: Space Physics*, *119*(9), 7501–7521. <https://doi.org/10.1002/2014JA020264>
- Skjæveland, S. S., Carlson, H. C., & Moen, J. I. (2017). A statistical survey of heat input parameters into the cusp thermosphere. *Journal of Geophysical Research: Space Physics*, *122*(9), 9622–9651. <https://doi.org/10.1002/2016JA023594>
- Smith, A. M., Mitchell, C. N., Watson, R. J., Meggs, R. W., Kintner, P. M., Kauristie, K., & Honary, F. (2008). GPS scintillation in the high arctic associated with an auroral arc. *Space Weather*, *6*(3), S03D01. <https://doi.org/10.1029/2007SW000349>
- Sojka, J. J., Bowline, M. D., Schunk, R. W., Decker, D. T., Valladares, C. E., Sheehan, R., et al. (1993). Modeling polar cap F-region patches using time varying convection. *Geophysical Research Letters*, *20*(17), 1783–1786. <https://doi.org/10.1029/93GL01347>
- Spicher, A., Cameron, T., Grono, E. M., Yakymenko, K. N., Buchert, S. C., Clausen, L. B. N., et al. (2015). Observation of polar cap patches and calculation of gradient drift instability growth times: A swarm case study. *Geophysical Research Letters*, *42*(2), 201–206. <https://doi.org/10.1002/2014GL062590>
- Spicher, A., Deshpande, K., Jin, Y., Oksavik, K., Zettergren, M. D., Clausen, L. B. N., et al. (2020). On the production of ionospheric irregularities via Kelvin-Helmholtz instability associated with cusp flow channels. *Journal of Geophysical Research: Space Physics*, *125*(6), e2019JA027734. <https://doi.org/10.1029/2019JA027734>
- Spogli, L., Alfonsi, L., De Franceschi, G., Romano, V., Aquino, M. H. O., & Dobson, A. (2009). Climatology of GPS ionospheric scintillations over high latitude and mid-latitude European regions. *Annals of Geophysics*, *27*(9), 3429–3437. <https://doi.org/10.5194/angeo-27-3429-2009>
- St.-Maurice, J.-P., & Hanson, W. B. (1982). Ion frictional heating at high latitudes and its possible use for an in situ determination of neutral thermospheric winds and temperatures. *Journal of Geophysical Research*, *87*(A9), 7580–7602. <https://doi.org/10.1029/ja087ia09p07580>
- SuperDARN. (2021). SuperDARN 2013 RAWACF. <https://doi.org/10.20383/102.0449>
- SuperDARN Data Analysis Working Group. (2022). Superdarn radar software toolkit (RST) 5.0. <https://doi.org/10.5281/zenodo.7467337>
- SuperDARN Data Visualization Working Group. (2024). Superdarn/pydarn: Pydarn v4.0. *Zenodo*. <https://doi.org/10.5281/zenodo.10452339>
- Thayyil, J. P., McCaffrey, A. M., Wang, Y., Themens, D. R., Watson, C., Reid, B., et al. (2021). Global positioning system (GPS) scintillation associated with a polar cap patch. *Remote Sensing*, *13*(10), 1915. <https://doi.org/10.3390/rs13101915>
- Tsunoda, R. T. (1988). High-latitude F region irregularities: A review and synthesis. *Reviews of Geophysics*, *26*(4), 719–760. <https://doi.org/10.1029/RG026i004p00719>
- Valladares, C. E., Basu, S., Buchau, J., & Friis-Christensen, E. (1994). Experimental evidence for the formation and entry of patches into the polar cap. *Radio Science*, *29*(1), 167–194. <https://doi.org/10.1029/93RS01579>
- van der Meeren, C., Oksavik, K., Lorentzen, D. A., Rietveld, M. T., & Clausen, L. B. N. (2015). Severe and localized GNSS scintillation at the poleward edge of the nightside auroral oval during intense substorm aurora. *Journal of Geophysical Research: Space Physics*, *120*(12), 10607–10621. <https://doi.org/10.1002/2015JA021819>
- Van Dierendonck, A., Klobuchar, J., & Hua, Q. (1993). Ionospheric scintillation monitoring using commercial single frequency c/a code receivers. In *Proceedings of the 6th international technical meeting of the satellite division of the Institute of navigation (ION GPS 1993)* (pp. 1333–1342). Retrieved from <http://clare.mysds.me/NOVATEL/Documents/Papers/File13.pdf>
- Vierinen, J., Coster, A. J., Rideout, W. C., Erickson, P. J., & Norberg, J. (2016). Statistical framework for estimating GNSS bias. *Atmospheric Measurement Techniques*, *9*(3), 1303–1312. <https://doi.org/10.5194/amt-9-1303-2016>

- Vonrat-Reberac, A., Fontaine, D., Blelly, P.-L., & Galand, M. (2001). Theoretical predictions of the effect of cusp and dayside precipitation on the polar ionosphere. *Journal of Geophysical Research*, *106*(A12), 28857–28865. <https://doi.org/10.1029/2001JA900131>
- Wannberg, G., Wolf, I., Vanhainen, L., Koskenniemi, K., Röttger, J., Postila, M., et al. (1997). The EISCAT Svalbard radar: A case study in modern incoherent scatter radar system design. *Radio Science*, *32*(6), 2283–2307. <https://doi.org/10.1029/97RS01803>
- Weber, E. J., Buchau, J., Moore, J. G., Sharber, J. R., Livingston, R. C., Winningham, J. D., & Reinisch, B. W. (1984). F layer ionization patches in the polar cap. *Journal of Geophysical Research*, *89*(A3), 1683–1694. <https://doi.org/10.1029/JA089iA03p01683>
- World Data Center for Geomagnetism, Kyoto. (2015). Geomagnetic AE index. Retrieved from. <https://doi.org/10.17593/15031-54800>
- World Data Center for Geomagnetism, Kyoto. (2022). Mid-latitude geomagnetic indices ASY and SYM (ASY/SYM indices). Retrieved from <http://hdl.handle.net/2433/267216>
- Yang, Z., Morton, Y. T. J., Zakharenkova, I., Cherniak, I., Song, S., & Li, W. (2020). Global view of ionospheric disturbance impacts on kinematic gps positioning solutions during the 2015 st. patrick's day storm. *Journal of Geophysical Research: Space Physics*, *125*(7), e2019JA027681. <https://doi.org/10.1029/2019JA027681>
- Yeh, K. C., & Liu, C.-H. (1982). Radio wave scintillations in the ionosphere. *Proceedings of the IEEE*, *70*(4), 324–360. <https://doi.org/10.1109/PROC.1982.12313>
- Zhang, Q.-H., Zhang, B.-C., Liu, R.-Y., Dunlop, M. W., Lockwood, M., Moen, J., et al. (2011). On the importance of interplanetary magnetic field by on polar cap patch formation. *Journal of Geophysical Research*, *116*(A5), A05308. <https://doi.org/10.1029/2010JA016287>
- Zheng, Y., Xiong, C., Jin, Y., Liu, D., Oksavik, K., Xu, C., et al. (2022). The refractive and diffractive contributions to GPS signal scintillation at high latitudes during the geomagnetic storm on 7–8 September 2017. *Journal of Space Weather and Space Climate*, *12*, 40. <https://doi.org/10.1051/swsc/2022036>